Article:
Ren, Y, Stuart, G, Houseman, G et al. (26 more authors) (2013) Crustal structure of the carpathian-pannonian region from ambient noise tomography. Geophysical Journal International, 195 (2). 1351 - 1369. ISSN 0956-540X

https://doi.org/10.1093/gji/ggt316

Geophysical Journal International

Geophys. J. Int. (2013) **195,** 1351–1369
Advance Access publication 2013 September 6

doi: 10.1093/gji/ggt316

Crustal structure of the Carpathian–Pannonian region from ambient noise tomography

Yong Ren,[1] Bogdan Grecu,[2] Graham Stuart,[1] Gregory Houseman,[1] Endre Hegedüs[3] and South Carpathian Project Working Group

[1]*School of Earth and Environment, University of Leeds, Leeds, LS2 9JT, UK. E-mail: earyr@leeds.ac.uk*
[2]*National Institute of Earth Physics, P.O. Box MG-21, Bucharest-Magurele, Romania*
[3]*Eötvös Loránd Geophysical Institute,* 1145 *Budapest, Kolumbusz u.* 17-23, *Hungary*

Accepted 2013 August 5. Received 2013 June 3; in original form 2013 January 18

SUMMARY

We use ambient noise tomography to investigate the crust and uppermost mantle structure beneath the Carpathian–Pannonian region of Central Europe. Over 7500 Rayleigh wave empirical Green's functions are derived from interstation cross-correlations of vertical component ambient seismic noise recordings (2005–2011) using a temporary network of 54 stations deployed during the South Carpathian Project (2009–2011), 56 temporary stations deployed in the Carpathian Basins Project (2005–2007) and 100 permanent and regional broad-band stations. Rayleigh wave group velocity dispersion curves (4–40 s) are determined using the multiple-filter analysis technique. Group velocity maps are computed on a grid of $0.2^\circ \times 0.2^\circ$ from a non-linear 2-D tomographic inversion using the subspace method. We then inverted the group velocity maps for the 3-D shear wave velocity structure of the crust and uppermost mantle beneath the region. Our shear wave velocity model provides a uniquely complete and relatively high-resolution view of the crustal structure in the Carpathian–Pannonian region, which in general is validated by comparison with previous studies using other methods to probe the crustal structure. At shallow depths (<10 km) we find relatively high velocities below where basement is exposed (e.g. Bohemian Massif, Eastern Alps, most of Carpathians, Apuseni Mountains and Trans-Danubian Ranges) whereas sedimentary areas (e.g. Vienna, Pannonian, Transylvanian and Foçsani Basins) are associated with low velocities of well defined depth extent. The mid to lower crust (16–34 km) below the Mid-Hungarian Line is associated with a broad NE–SW trending relatively fast anomaly, flanked to the NW by an elongated low-velocity region beneath the Trans-Danubian Ranges. In the lowermost crust and uppermost mantle (between 30 and 40 km), relatively low velocities are observed beneath the Bohemian Massif and Eastern Alps but the most striking features are the broad low velocity regions beneath the Apuseni Mountains and most of the Carpathian chain, which likely is explained by relatively thick crust. Finally, most of the Pannonian and Vienna Basin regions at depths >30 km are relatively fast, presumably related to shallowing of the Moho consequent on the extensional history of the Pannonian region.

Key words: Surface waves and free oscillations; Seismic tomography; Crustal structure; Europe.

1 INTRODUCTION

The Carpathian–Pannonian region in Central Europe, consists of the Pannonian Basin surrounded by the Alpine, Carpathian and Dinaric mountain belts (Fig. 1). These topographic features developed as a consequence of the continental collision between the Adriatic microplate and the European continent, which began in the Late Mesozoic (Royden *et al.* 1982; Horváth *et al.* 2006). The pre-Tertiary basement of the Pannonian Basin is made up of two main structural domains: Alcapa in the northwest and Tisza-Dacia in the southeast (Fig. 1). The Alcapa unit includes the nappe system of the northeastern edge of the Alps, the Little Hungarian Plain and Transdanubian ranges, and is bounded by the Pieniny Klippen belt to the north and the Balaton line to the south (Kovács & Haas 2011). The Tisza-Dacia block is comprised of two subunits: the Tisza block underlying most of the Great Hungarian Plain, and the Dacia block comprising the Transylvanian Basin, bounded by the East Carpathian and South Carpathian mountain ranges (Csontos &

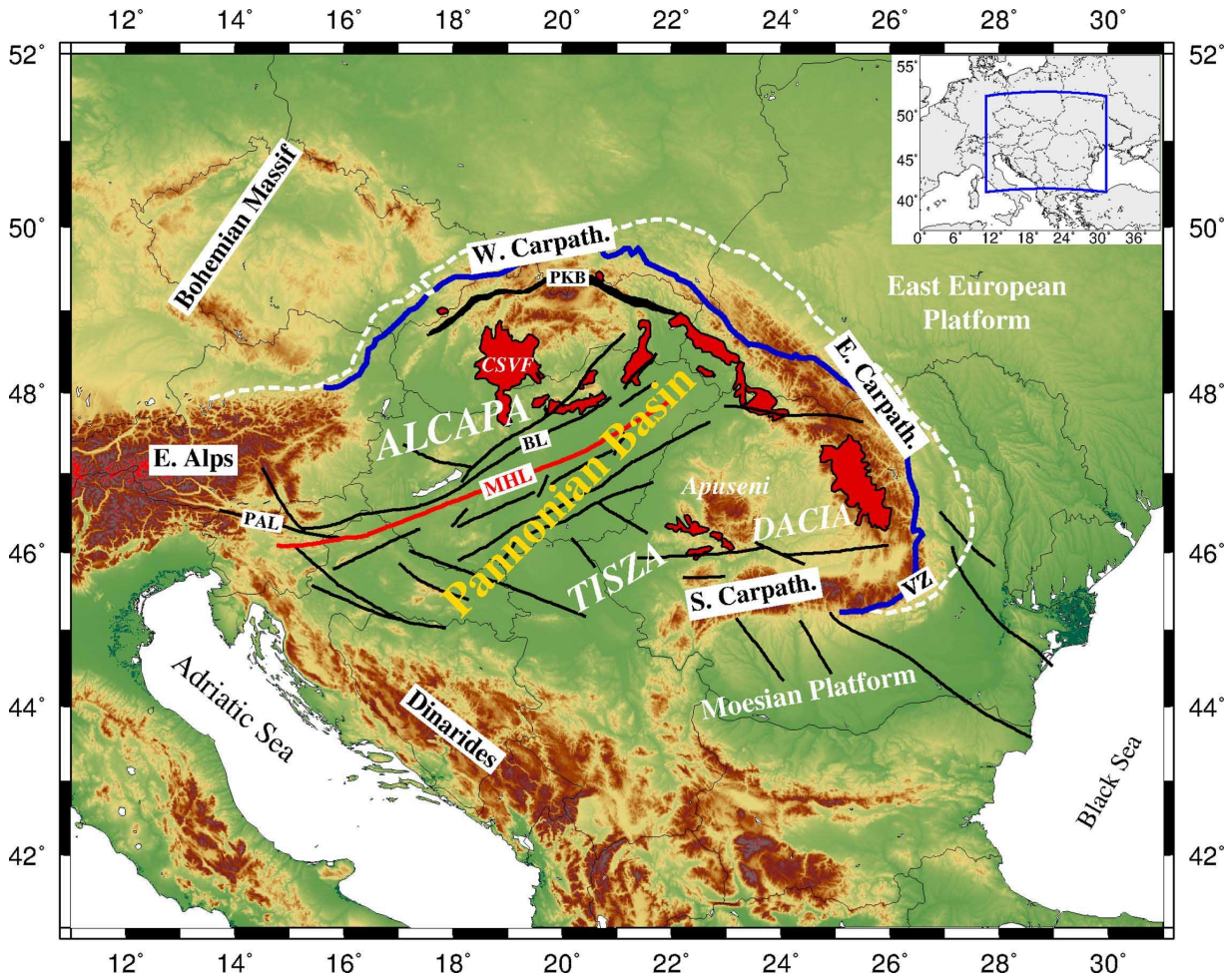

Figure 1. Topographic map of the Carpathian–Pannonian system with surface structural features: red filled patterns indicate outcrops of calc-alkaline and silicic volcanic rocks after Harangi & Lenkey (2007); black lines show some of the major faults. CSVF, Central Slovakian volcanic field; PAL, Peri-Adriatic Line; MHL, Mid-Hungarian Line; BL, Balaton Line; PKB, Pieniny Klippen Belt; VZ, Vrancea Zone.

Vörös 2004). During the Neogene, the Alcapa unit underwent a net counter-clockwise rotation of about 50°–70° and was translated to the ENE (Márton & Fodor 1995), whereas the Tisza-Dacia unit rotated clockwise 90° (Pâtraşcu *et al.* 1994). The rotation of these two blocks was accompanied by extension during the Miocene, which led to the formation of the Pannonian Basin. Several theories proposed to explain the formation of this basin include extension due to the eastward rollback of a subducted slab (Horváth *et al.* 1993, 2006) and/or gravitational collapse of former overthickened orogenic terrain (Gemmer & Houseman 2007). The Pannonian Basin includes a set of small, deep subbasins (some can exceed 7 km in thickness), separated by relatively shallow basement blocks and filled with Neogene-Quaternary sediments (Tari *et al.* 1999).

Constraining crustal and lithospheric structures in the Carpathian–Pannonian region is crucial for a better understanding of the dynamic processes that determined the tectonic evolution of the region. Previous seismological investigations of the crustal structure in the region are mainly based on controlled-source seismic reflection/refraction studies on 2-D profiles. There is reasonable control on crustal structure in the western part of the Carpathian–Pannonian region from CELEBRATION 2000 (Guterch *et al.* 2003; Grad *et al.* 2008), ALP 2002 (Brückl *et al.* 2003; Behm *et al.* 2007) and SUDETES 2003 (Grad *et al.* 2003, 2008) seismic experiments. In contrast, the eastern part of the Carpathian–Pannonian region has limited coverage with the VRANCEA 2001 refraction line (Hauser *et al.* 2007), the combined DRACULA I and DACIA-PLAN reflection line (Fillerup *et al.* 2010) crossing the Transylvanian Basin, Vrancea Zone and Foçsani Basin. 3-D seismic velocity models for the Vrancea region incorporating converted phase measurements from local and teleseismic sources have also been developed by Martin *et al.* (2005) and Ivan (2011). Although those studies provide important measurements of crustal structure which have been influential in geodynamic interpretations, other parts of the region (for example, the Apuseni Mountains of Romania) are almost unconstrained by seismic measurements of the crust. To date, the available regional crustal models (e.g. Bassin *et al.* 2000; Tesauro *et al.* 2008; Grad *et al.* 2009) are essentially based on a sparse network of refraction lines interpolated across the unsampled regions. Surface wave tomography, derived from ambient seismic noise analysis, represents an alternative seismic technique that provides important new, relatively high-resolution, constraints on the 3-D crustal structure of the region.

Ambient noise tomography has proven particularly powerful in imaging the Earth's crust and uppermost mantle in the last decade, at both regional and global scale beneath dense seismic arrays (e.g. Shapiro *et al.* 2005; Yao *et al.* 2006; Lin *et al.* 2007; Moschetti *et al.* 2007; Yang *et al.* 2007; Li *et al.* 2009; Arroucau *et al.* 2010; Saygin & Kennett 2012). The technique is based on the principle that an estimate of surface wave Green's functions between two stations can be retrieved from cross-correlation of ambient seismic noise

records (Weaver & Lobkis 2001; Derode *et al.* 2003; Snieder 2004; Wapenaar 2004; Larose *et al.* 2005). Ambient noise tomography has the advantage of not depending on the distribution of earthquake sources as in classical interstation surface wave tomography; even if the noise is anisotropic, resolution is essentially limited by the distribution of stations and the frequencies present in the seismic wavefield. The short to intermediate-period dispersion curve measurements that constrain the crust and uppermost mantle structures, can be more effectively retrieved from ambient noise analysis than from the surface wave signals of seismic events. Here, we present Rayleigh-wave group velocity maps for period range 4–40 s, and interpret crustal and uppermost mantle shear wave velocity structures from ambient noise tomography, using data from a uniquely dense network of permanent and temporary broad-band seismic stations in the Carpathian–Pannonian region.

2 DATA PROCESSING AND MEASUREMENT

2.1 Data

We assembled continuous broad-band vertical component seismic data recorded on 207 stations in the Carpathian–Pannonian region (Fig. 2) from four sources: South Carpathian Project (SCP, 2009–2011, Ren *et al.* 2012), Carpathian Basins Project (CBP, 2005–2007; Dando *et al.* 2011), Romanian National Seismic Network (http://www.infp.ro) and other permanent stations available from international data centres. The South Carpathian Project was a major collaborative seismological project between the University of Leeds, Eötvös Loránd Geophysical Institute (ELGI), Budapest, Hungary; National Institute of Earth Physics (NIEP), Bucharest, Romania and the State Seismological Survey of Serbia (RSZ), Belgrade, Serbia. The SCP temporary network (Fig. 2) consisted of 17 CMG-40T, 13 CMG-3T and 24 CMG-6TD sensors, installed across the eastern Pannonian Basin, Transylvanian Basin and the South Carpathian Mountains in Hungary, Romania and Serbia, between June 2009 and June 2011 (Ren *et al.* 2012). The Carpathian Basins Project was a collaborative seismic experiment deployed by University of Leeds, ELGI, RSZ and TU-Wien (Technische Universität Wien, Austria) between October 2005 and August 2007. The CBP temporary network (Fig. 2) consisted of 46 CMG-6TD and 10 CMG-3T(D) sensors, installed across Eastern Austria, Western Hungary, Northern Serbia and Croatia (Dando *et al.* 2011). Three of these broad-band stations were in operation during the whole period covering both the CBP and SCP experiments. We have also used data from 30 broad-band temporary and permanent stations of

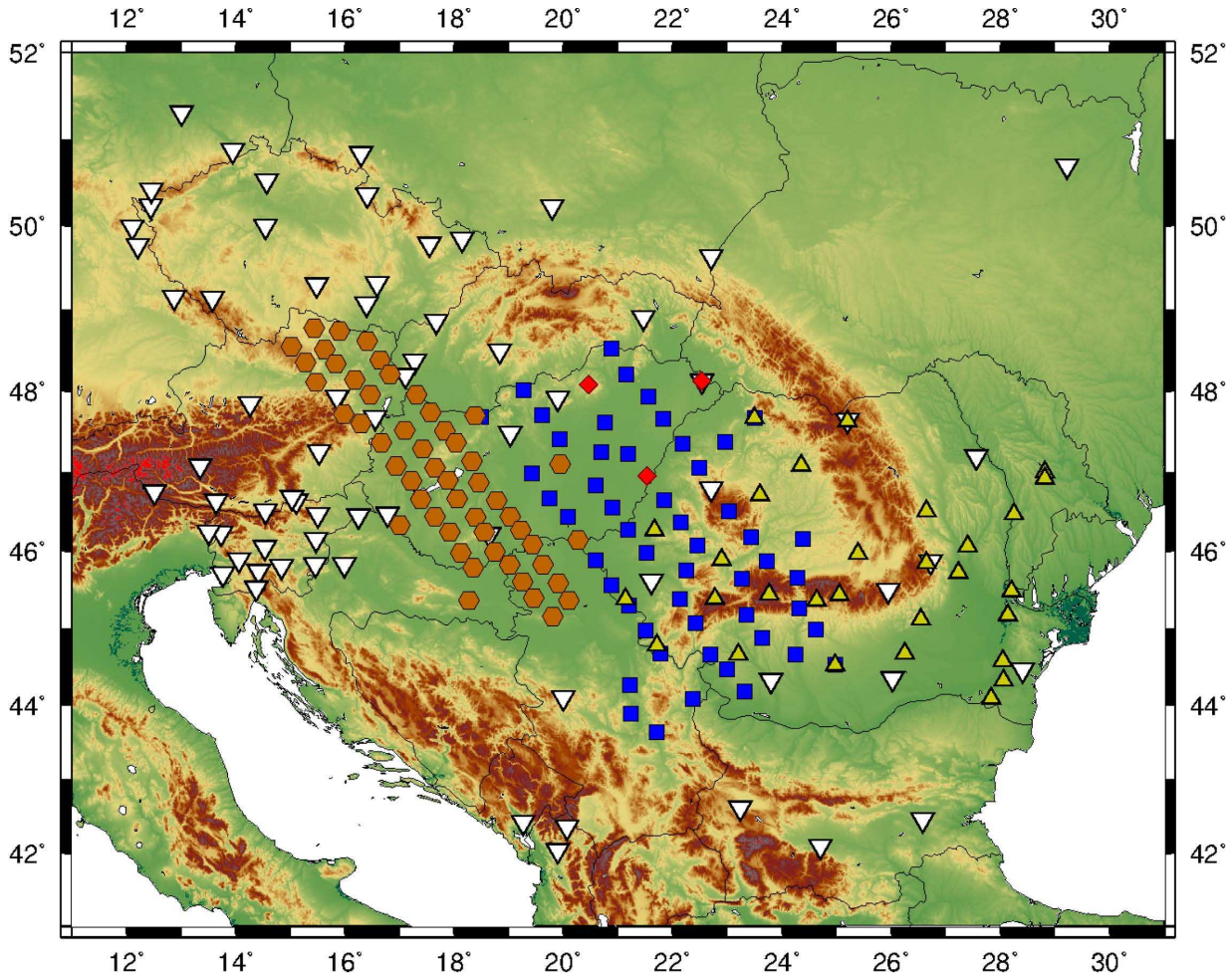

Figure 2. Distribution of broad-band stations used in this study. Blue squares represent stations of the temporary network deployed in the South Carpathian Project (SCP, 2009–2011; Ren *et al.* 2012). Brown hexagons mark stations from the temporary network deployed in the Carpathian Basins Project (CBP, 2005–2007; Dando *et al.* 2011). Red diamonds represent stations which were in operation in both CBP and SCP experiments. White inverted triangles depict additional permanent broad-band stations used in this study. Yellow triangles represent seismic stations from the Romanian Regional Seismic Network (http://www.infp.ro).

the Romanian National Seismic Network, operated by the National Institute of Earth Physics, Bucharest, Romania and from 70 permanent broad-band stations in the Carpathian–Pannonian region obtained from Incorporated Research Institutions for Seismology (IRIS), Observatories and Research Facilities for European Seismology (Orfeus) and GFZ Seismological data archives. Many of the broad-band seismic stations used in our ambient noise tomography have a flat instrument response out to 120 s, enabling extraction of surface waves up to those periods. However, data from CMG-6TD sensors from SCP and CBP temporary deployments, which represent about one third of the total number of stations, have a relatively low signal-to-noise ratio and a flat response only to periods of about 30 s. In this study, the number of dispersion measurements at longer periods is restricted by the aperture of our station network, so we decided to focus our ambient noise tomographic analysis in the period range 4–40 s, which basically restricts our focus to the crust and perhaps the upper few tens of kilometres of the mantle.

2.2 Estimate of Rayleigh-wave Green's functions

We have used continuous vertical component seismograms to obtain two-station cross-correlation functions on day-length waveforms to estimate Rayleigh-wave Green's functions. The raw data had first their instrument response, mean and trend removed. The resulting time series were then tapered, bandpass filtered between periods of 4 and 60 s and resampled to 1 sps (sample per second). The cross-correlations are undertaken after one-bit normalization (Bensen *et al.* 2007) to reduce the contamination of the Green's function by actual earthquake waveforms or other incoherent noise as follows:

$$C_{\mathrm{AB}}(t) = \int_0^T \mathrm{sgn}[\nu_A(\tau)] \cdot \mathrm{sgn}[\nu_{\mathrm{B}}(\tau + t)]\mathrm{d}\tau, \tag{1}$$

where C_{AB} is the cross-correlation function between stations A and B, $\nu_{\mathrm{A}}(t)$ and $\nu_{\mathrm{B}}(t)$ correspond to the continuous data recorded at the stations A and B, repectively, and T is the time period for the cross-correlation. The cross-correlation functions for different interstation paths are then stacked over a period of 1–2 yr for the temporary stations and over 5 yr for permanent stations. We also averaged the positive and negative lag waveforms obtained from the cross-correlations in order to reduce the effects of inhomogeneity of the seismic noise source distribution (Yang *et al.* 2007). This 'symmetric-signal' is finally used to obtain the estimated Rayleigh-wave Green's function by taking its time derivative and multiplying by -1.

$$G_{\mathrm{AB}}(t) = -\frac{\mathrm{d}\overline{C_{\mathrm{AB}}(t)}}{\mathrm{d}t}, \tag{2}$$

where G_{AB} is the estimated Green's function of the Rayleigh wave propagating between stations A and B, and $\overline{C_{\mathrm{AB}}(t)}$ is the average of positive and negative lag cross-correlation functions.

Contrary to previous studies (e.g. Shapiro *et al.* 2005; Yao *et al.* 2006; Lin *et al.* 2007; Moschetti *et al.* 2007; Yang *et al.* 2007; Li *et al.* 2009; Arroucau *et al.* 2010; Saygin & Kennett 2012) which generally use a standard linear stacking method to extract surface wave Green's functions, we applied here the time-frequency domain phase-weighted stacking technique (tf-PWS) developed by Schimmel *et al.* (2010) to our cross-correlation functions. This technique has been shown to improve considerably the signal-to-noise ratio of the empirical Green's function in the stacking process. We compared the tf-PWS technique and the standard linear stacking technique on different interstation paths, and our comparison confirms that the tf-PWS stacking technique yields much cleaner Green's functions (Schimmel *et al.* 2010) (Fig. 3). Fig. 4(b) shows for example our final estimated Rayleigh-wave Green's functions propagating between the station ARSA and all other stations, bandpass filtered between 10 and 20 s.

2.3 Group velocity dispersion measurements

We apply the frequency-time analysis (FTAN) multiple-filter technique (Dziewonski *et al.* 1969) to measure the group velocity dispersion curves in the period range 4–40 s from the estimated Rayleigh wave Green's function (Fig. 4d). We have studied over 13 354 interstation paths with a distance ranging from 20 to 1450 km. The Gaussian filter operator, used in the FTAN technique, is described by $\exp[-\alpha(f - f_{\mathrm{c}})^2/f_{\mathrm{c}}^2]$, where α determines the frequency resolution of the filter and f_{c} is the centre frequency. Following Cho *et al.* (2007), we have explored a wide range of values for α and found that the best values for our study are between 5.0 and 20.0, depending on the interstation distance. Yang *et al.* (2007) pointed out that the stations must be separated by at least three wavelengths to obtain a reliable dispersion curve measurement, and as such, each dispersion curve is used only for periods less than one third of the observed traveltime. The number of dispersion curve measurements used ranges from 2219 for 40 s period to 7267 for 10 s period. Fig. 4(e) shows the distribution of the number of measurements as a function of the period. For the shortest and longest periods ($T \leq 5$ s and $T > 25$ s), the number of measurements decreases significantly as waveforms with poor signal-to-noise ratio are discarded.

3 GROUP VELOCITY TOMOGRAPHY

We construct group velocity maps from the estimated Rayleigh wave Green's functions at periods from 4 to 40 s (with increment of 1 s), using the non-linear 2-D tomographic inversion technique developed by Rawlinson & Sambridge (2003). Traveltimes through the 2-D model are computed using the fast marching algorithm of Sethian & Popovici (1999), in which a finite-difference method is used to solve the eikonal equation. This technique has some advantages over ray tracing methods as it is more stable, and successfully finds the first-arrival and diffraction paths in shadow zones. The inversion procedure uses a gradient method based on the subspace technique (Kennett *et al.* 1988), where the minimization is carried out simultaneously along several search directions that together span a subspace of the model space (Rawlinson & Sambridge 2003, 2004a,b). The technique has been successfully used for ambient noise tomography in several regions (e.g. Arroucau *et al.* 2010; Saygin & Kennett 2012). We briefly describe the inversion procedure used here, but more details on the inversion technique can be found in Kennett *et al.* (1988), Williamson (1990) and Rawlinson & Sambridge (2003, 2004a,b).

3.1 Inversion method

The object of the tomographic inversion is to provide a model of the group velocity variation which best explains the interstation traveltimes. This goal is formulated as the minimization of an objective function $\mathbf{S(m)}$ consisting of a data residual term and two regularization terms:

$$\mathbf{S(m)} = \frac{1}{2}\Big\{[\mathbf{g(m)} - \mathbf{d}_{\mathrm{obs}}]^T \mathbf{C}_d^{-1}[\mathbf{g(m)} - \mathbf{d}_{\mathrm{obs}}] + \epsilon(\mathbf{m} - \mathbf{m}_0)^T \mathbf{C}_m^{-1}(\mathbf{m} - \mathbf{m}_0) + \eta \mathbf{m}^T \mathbf{D}^T \mathbf{D}\mathbf{m}\Big\} \tag{3}$$

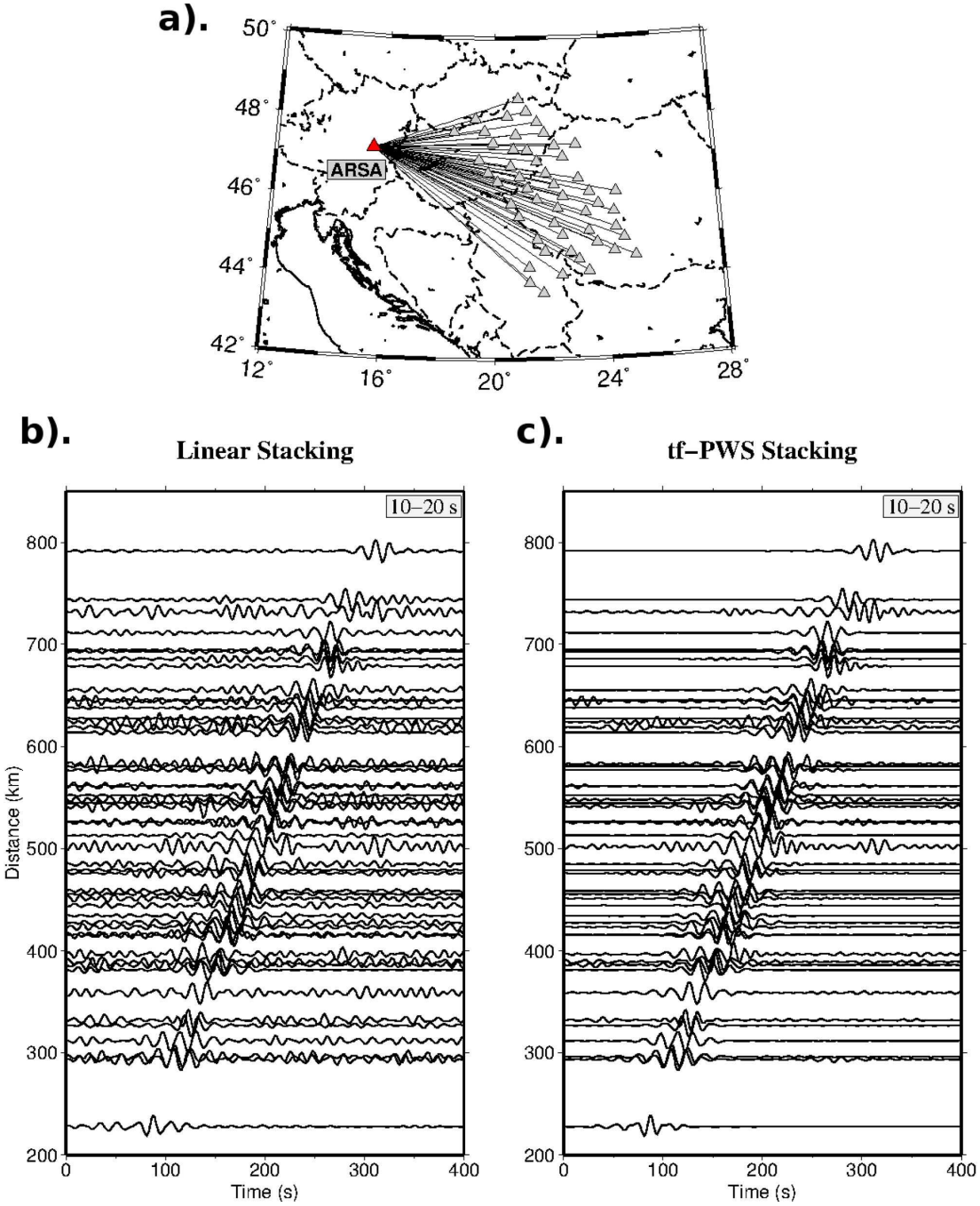

Figure 3. Examples of estimated Rayleigh wave Green's functions for paths between the station ARSA and SCP temporary stations (a) constructed using the linear stacking technique (b) and using the tf-PWS stacking technique (c).

where $\mathbf{g}(\mathbf{m})$ represents the predicted group traveltimes from the model $\mathbf{m}$, $\mathbf{m}_0$ is an initial estimate of the model, $\mathbf{d}_{\rm obs}$ is a vector of the observed group traveltimes, $\mathbf{C}_{\rm d}$ is the data covariance matrix for which we assume a diagonal matrix with variances based on a uniform traveltime uncertainty of 2 s, $\mathbf{C}_{\rm m}$ is the *a priori* model covariance matrix for which we assume a diagonal matrix with uniform *a priori* variances based on a model parameter uncertainty of $0.3\,{\rm km\,s^{-1}}$, $\mathbf{D}$ is the derivative operator which has the role of smoothing the model, ϵ and η are respectively, the damping and smoothing parameters. These choices of the variance estimates are only approximate. The significant point is that we assume they are of uniform magnitude.

Following Rawlinson & Sambridge (2003), the minimization of the objective function is performed using an iterative approach to overcome the non-linearity of $\mathbf{g}$

$$\mathbf{m}_{n+1} = \mathbf{m}_n + \delta\mathbf{m}, \tag{4}$$

where $\delta\mathbf{m}$ is found iteratively using the subspace method. At each iteration, the subspace method restricts the minimization of the

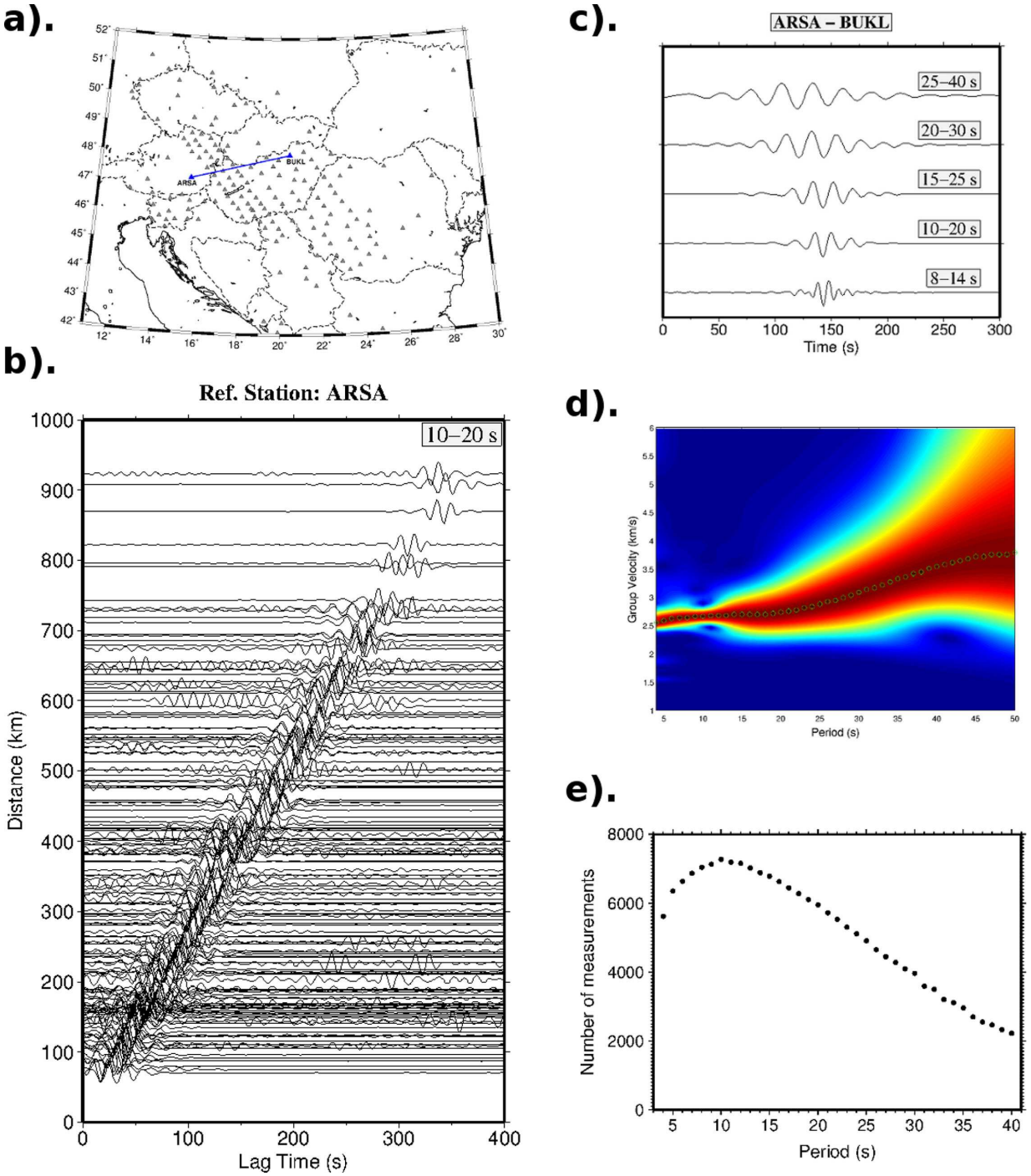

Figure 4. (a) Map showing the location of all stations and the path between the stations ARSA and BUKL. (b) Example of extracted interstation Rayleigh wave Green's functions filtered at period 10–20 s, where ARSA is the reference station. (c) An example of estimated Green's function of Rayleigh wave for the path ARSA-BUKL. (d) Example of frequency–time analysis (FTAN) diagram showing Rayleigh wave group velocity for the path ARSA-BUKL. (e) Diagram representing the total number of path measurements as a function of period.

objective function $\mathbf{S}(\mathbf{m})$ to a p-dimensional subspace of the model space, thus the perturbation $\delta\mathbf{m}$ is an element of the space spanned by a set of p M-dimensional basis vectors $\{\mathbf{a}^j\}$

$$\delta\mathbf{m} = \sum_{j=1}^{p} \mu_j \mathbf{a}^j = \mathbf{A}\mu, \tag{5}$$

where $\mathbf{A} = [\mathbf{a}^j]$ is the $M \times p$ projection matrix. The component μ determines the length of the corresponding vector $\mathbf{a}^j$ that minimizes the objective function $\mathbf{S}(\mathbf{m})$ in the space spanned by $\mathbf{a}^j$. In this implementation, the final expression for the model update can be written as

$$\delta\mathbf{m} = -\mathbf{A}\left[\mathbf{A}^T(\mathbf{G}^T\mathbf{C}_d^{-1}\mathbf{G} + \epsilon\mathbf{C}_m^{-1} + \eta\mathbf{D}^T\mathbf{D})\mathbf{A}\right]^{-1}\mathbf{A}^T\hat{\gamma}, \tag{6}$$

where $\hat{\gamma}$ is the current data misfit and $\mathbf{G}$ is the linearized approximation to the gradient of $\mathbf{g}(\mathbf{m})$. After each update of the model by (4), the surface waves are retraced through the amended model

using the fast marching method, and then the terms **A**, $\hat{\gamma}$ and **G** are re-evaluated. The final group velocity models presented in this paper are obtained after eight iterations of the inversion at which point the model update is small.

The region of interest in our study is $20^\circ \times 11^\circ$ (Fig. 1). We parametrized the area using a $0.2^\circ \times 0.2^\circ$ grid of 5656 nodes where velocities are smoothly interpolated with the bicubic B-spline between nodes to form a continuous group velocity field. The reference velocity model used to damp the inversion (3) is the current average velocity at the relevant period. We ran the inversion using a range of damping and smoothing parameters ($0 < \varepsilon, \eta < 5000$) to determine their optimal values. There is little significant difference between the various group velocity maps produced with different regularization parameters; we present maps based on what we judge to be optimum parameters (for damping $\varepsilon = 10$, for smoothing $\eta = 60$).

3.2 Resolution tests

We performed checkerboard resolution tests to assess the reliability of the tomographic inversion. The input synthetic checkerboard velocity model consists of alternating cells ($0.6^\circ \times 0.6^\circ$) of opposite sign with a maximum velocity perturbation of 0.5 km s^{-1} relative to the reference velocity. Between neighbouring anomalies, null anomalies of similar size are defined. Synthetic group-velocity traveltime residuals were computed between the same station pairs used in the observed data set using the fast marching method. Data noise was not simulated in these tests. Fig. 5 shows the retrieved velocity models from these tests for periods of 6, 10 and 20 s. The checkerboard tests (Fig. 5), show that our inversion can adequately resolve structures as small as 60 km in most of the Carpathian–Pannonian region, with some degradation or smearing of the recovered solutions near the edges of the station distribution map.

3.3 Depth sensitivity of Rayleigh group wave

Surface waves at different periods are sensitive to structures at different depths. Fig. 6 shows the depth dependence of shear wave velocity sensitivity kernels for Rayleigh wave group velocity at periods of 6, 10, 15, 25, 30 and 40 s, constructed using a modified version of the AK135 model (Herrmann & Ammon 2004). The short period Rayleigh waves (4–10 s) are particularly sensitive to the sedimentary overburden and the shallower upper crust (to ∼10 km depth). For the mid-period Rayleigh waves (10–20 s), the dominant sensitivity is at the mid-crustal depths (10–20 km); whereas the longer period (20–30 s) Rayleigh waves are most sensitive to velocities in the lower crust and uppermost mantle (20–40 km). Within our data set, only the Rayleigh waves at period 30–40 s constrain the deepest part of the lower crust and uppermost mantle (30–60 km).

4 GROUP VELOCITY MAPS

The Rayleigh-wave group velocity maps produced using our tomographic analysis, for periods of 6, 10, 15, 20, 25 and 30 s, are shown in Fig. 7. The group velocity maps at short periods (e.g. 6 and 10 s maps in Fig. 7) show coherent high and low velocity features, which accord well with surface tectonic features. At 6 s, high velocities are dominant where crystalline rocks outcrop. High velocities are observed beneath the Bohemian Massif and the Eastern Alps on Rayleigh-wave group velocity maps for periods up to about 20 s (Figs 7a–d); whereas the Transdanubian Ranges northwest of the Mid-Hungarian line and the West Carpathians present high velocities only to about 10 s periods. For the Southeast Carpathians high velocities are not present even at 6 s, although high velocities are observed further north in the East Carpathians and further west in the South Carpathians, most clearly in the period range 4–8 s (see 6 s map in Fig. 7). However, the low velocity features which dominate the southern half of the South Carpathians around the orocline are clearly affected by the great sediment thicknesses in Dacic and Foçsani Basins (Leever 2007).

The relatively low group velocities at periods up to about 15 s reflect mainly thick sediments. All known sedimentary depocentres in the Carpathian–Pannonian region (Fig. 8a) are identified by the low velocity regions in the 6 and 10 s group velocity maps (Figs 7a and b): the Békés and Makó Basins below the Great Hungarian Plain, Vienna and Danube Basins to the northwest, Drava Basin to the southwest, Transylvanian Basin in western Romania, Foçsani Basin east of the Vrancea zone and finally the foredeep Dacic Basin of the Moesian platform (refer to Figs 12 and 13 for location of these basins). However, the sediment thicknesses of these different basins are highly variable. The broad low velocity zones below the Pannonian Basins can be seen in our group velocity maps up to at least 12 s period (Figs 7a and b), but some slow anomalies persist even to 15 or 20 s period (Figs 7c and d). The Danube, Drava and Transylvanian basins are less deep and significantly low velocities are observed only to about 10 s. In contrast, low velocities persist to ∼25 s for the Vienna and Foçsani basins, as for the foredeep Dacic basin of the Moesian platform. These basins are also associated with relatively large negative free-air gravity anomalies (Fig. 8b), unlike most of the intra-Carpathian basins which have near zero free-air gravity anomalies.

At periods from 15 to 25 s (Figs 7c–e), group velocities become increasingly sensitive to crustal thickness; lower velocities imply thicker crust. The maps at these periods show low velocities beneath almost the entire Carpathian range (West, East and South) along with relatively high free-air gravity anomalies (Fig. 8b). The continuity of the low velocity anomaly below the East Carpathians seems to be interrupted near the border between Ukraine and Romania by a localized fast anomaly but this is one of the more poorly resolved locations in the solution (Fig. 5). The low velocities along the South Carpathians persist to ∼30 s period though the axis of low velocities is clearly offset to the south from the topographic axis of the South Carpathians. At periods from 30 to 40 s, we observe also the persistence of low velocities below the Apuseni Mountains, and the southeastern corner of the Carpathians. Although, the low velocities of the Carpathians can be interpreted as the signature of a deeper crustal root beneath the mountain belt, related to at least partial isostatic compensation, there is also a strong association in both West and East Carpathians with recent surface volcanism and high temperatures at shallow depths (e.g. Central Slovakia Volcanic Field, CSVF, in the West Carpathians (Szabó *et al.* 1992) and the bend zone of the East Carpathians (Seghedi *et al.* 2004)).

At 20–25 s period, our group velocity maps (Figs 7d and e) show a distinctly SW–NE elongated high velocity zone traversing the Pannonian region from the Eastern Alps in the SW, broadly aligned with the Mid-Hungarian Line. These higher velocities might be interpreted as a signature of crustal thinning. At greater periods (25–30 s) the Mid-Hungarian fast anomaly becomes more dominant, consistent with the idea of higher velocity mantle at shallower depth along this trend.

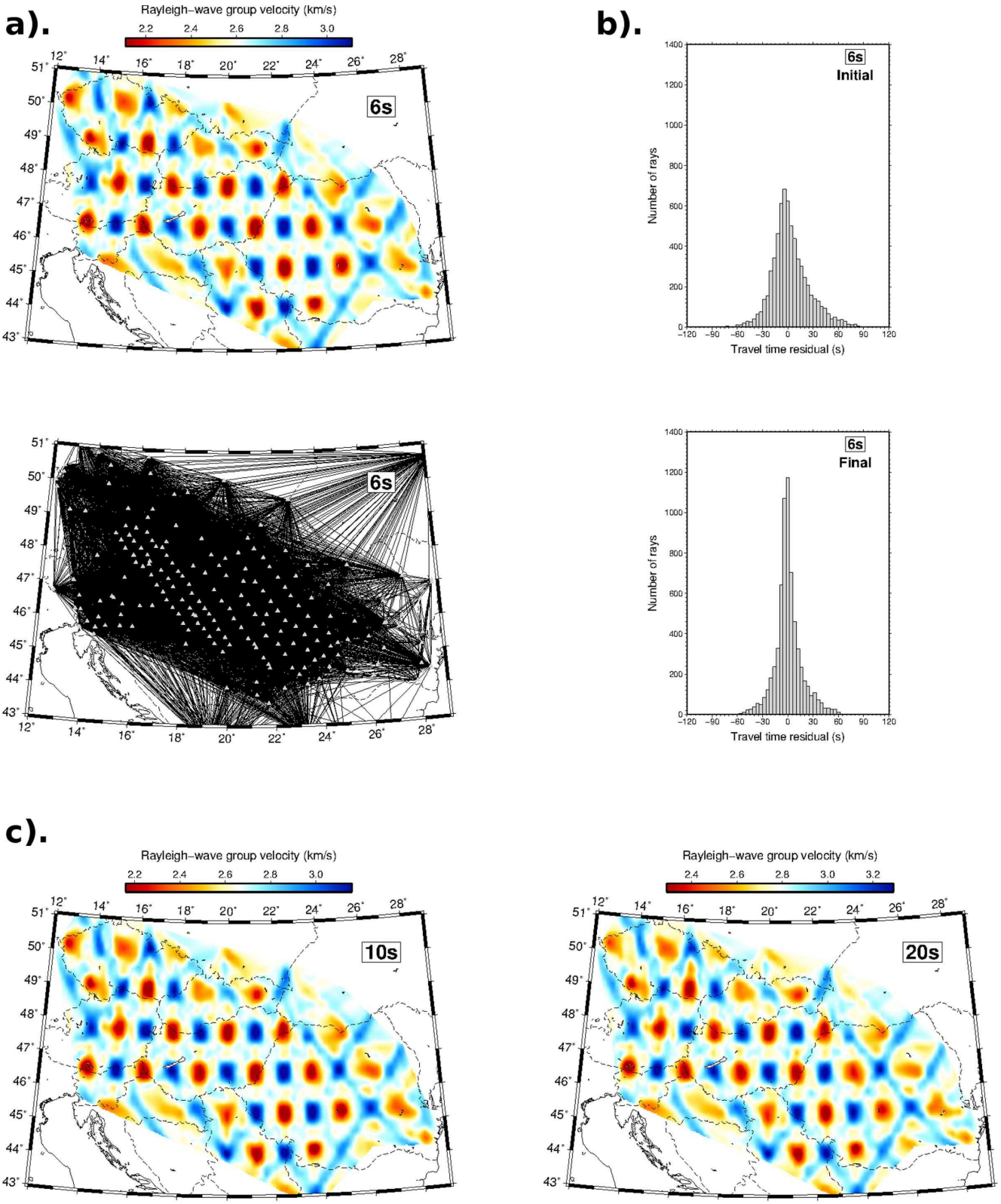

Figure 5. (a) Checkerboard resolution test and ray path coverage for the 6 s period map. For the resolution tests, the input anomalies of 0.6° × 0.6° have a maximum velocity perturbation of 0.5 km s^{-1} relative to a constant background velocity of 2.6 km s^{-1}. (b) Histograms of misfit for ambient noise data before (left-hand panels) and after (right-hand panels) inversion for the 6 s period. The group traveltime residuals rms has been reduced from 22.6 s before the inversion to 16.1 s after the inversion. (c) Checkerboard resolution tests for the 10 and 20 s periods.

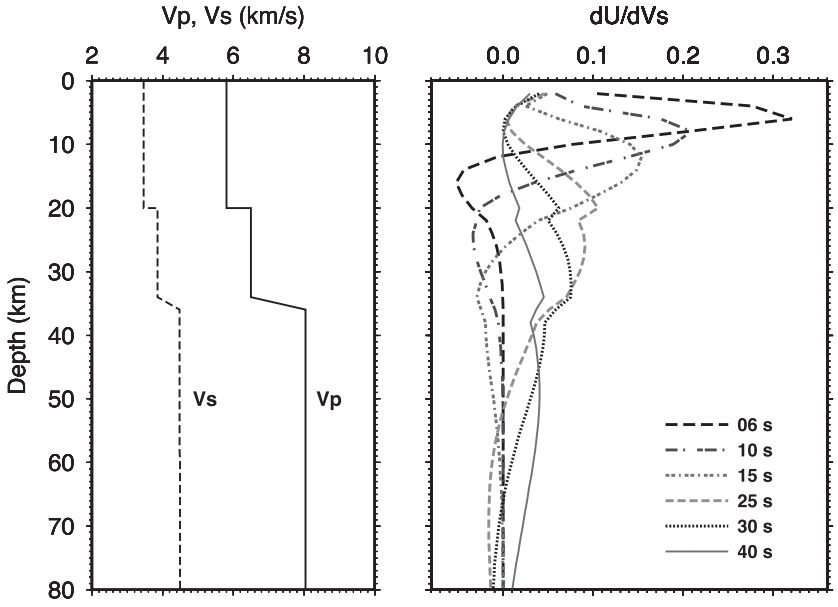

Figure 6. (a) *P*- and *S*-wave velocity models used for computing the depth sensitivity kernels of group velocity versus shear wave velocity. (b) Depth sensitivity kernels of fundamental mode Rayleigh wave group velocity to shear wave velocity for periods of 6, 10, 15, 25, 30 and 40 s.

5 *S*-WAVE VELOCITY STRUCTURE

From the group velocity maps determined previously, we extracted the group velocity dispersion curves at each grid node, smoothed using a best-fitting polynomial of degree 5. Inversions of dispersion curves for shear wave velocity versus depth at each grid node are then made using the program *surf96* developed by Herrmann & Ammon (2004). Our parametrization here assumed a 1-D layered Earth composed of 30 × 2-km-thick layers for the upper 60 km, above 4 × 5-km-thick layers to 80 km depth, above a half-space. In order to assess and reduce the influence of the starting velocities on the depth inversions, we carried out over 1000 inversions for each node using different initial *S*-wave velocity models for which velocity is either constant with depth (between 1.0 and 6.0 km s^{-1}) or linearly varying with depth from surface values between 1.0 and 6.0 km s^{-1} to the IASP91 value at 70 km depth. The corresponding initial *P*-wave velocities were scaled using the V_P/V_S ratios of the IASP91 model. Only models that yield a dispersion curve misfit $|\overline{\delta v}|$ less than 0.5 per cent of $\overline{v}$ were retained. The final shear wave velocity model is constructed by taking the median solution at each depth. The typical variation of derived inverted models is illustrated in Fig. 9 for selected nodes.

The structures in the resulting 3-D shear wave velocity model are similar to those observed in the group velocity maps, however, the depth extents of prominent features are now better defined. The group velocity models are more poorly resolved at longer period (>30 s) than at short and intermediate periods, because fewer group dispersion measurements are available. As a consequence, the short-wavelength structure in our *S*-wave models at depths >30 km is less reliable. To account for this depth-dependent resolution and to stabilize the depth inversion, we applied a depth-dependent spatial Gaussian filter to our *S*-wave velocity model. The filter is based on the radius of the first Fresnel zone: Williamson & Worthington (1993) suggested that the smallest feature that can appreciably influence a seismic wave is of the order of the first Fresnel zone radius $r_{\min} = \sqrt{\lambda L}$, where L is the propagation distance and $\lambda = v \cdot T$ the wavelength with v and T being the velocity and period of the surface wave. Using average surface wave velocities and average interstation distances (varying from 402 km at 6 s to 690 km at 40 s), we estimated $r_{\min}$ at each of the periods considered in this study. Since each period has its peak sensitivity at a specific depth (Fig. 6), we used $r_{\min}$ as a rough measure of the smallest heterogeneity that surface waves can resolve at that depth. We therefore define and apply to the solution a Gaussian filter $G(x, y) = \frac{1}{2\pi\sigma^2} \exp\left[-\frac{(x-x_0)^2+(y-y_0)^2}{2\sigma^2}\right]$ in which the horizontal averaging length σ, set to $r_{\min}$, increases with depth as shown in Figs 10(a). Fig. 10 compares the horizontally filtered and unfiltered *S*-wave velocity models for a horizontal slice at depth of 34 km (Fig. 10b), and for a vertical profile that spans the model (Fig. 10c).

Fig. 11 shows the final shear wave velocity model designated SCP-ANT-VS1 at depths of 2, 6, 10, 16, 30 and 40 km. An ASCII data file of nodal velocities for this model can be downloaded from the Supporting Information. Figs 12 and 13 show seven cross-sections across different parts of the Carpathian–Pannonian region. In the following section, we discuss these crustal velocity variations and what we can infer about the structure and tectonic history of three regions: (1) Bohemian Massif and Eastern Alps; (2) West Carpathians and Pannonian Basin System and (3) Transylvania and the East and South Carpathians, but first we summarize:

(i) Exposed basement in the Bohemian Massif, Eastern Alps, most of the Carpathian arc, the Apuseni Mountains and the Trans-Danubian Ranges explains high near-surface velocities in these regions (Figs 11a and b). In contrast thick sedimentary piles of the Danube, Vienna, Pannonian, Transylvanian, Foçsani and Dacic Basins produce near-surface low velocities. The low velocities associated with the Foçsani and Dacic Basins spill over into the SE Carpathians (Vrancea region) and across the Moesian Platform. The shallow low velocities in Vrancea may be related to recent volcanism in this region.

(ii) Into the mid-crust (10–16 km, Figs 11c and d) the Bohemian Massif and Eastern Alps remain relatively fast, but most of the Carpathians and the Trans-Danubian Range are now slow relative to surrounding regions, and the slow signature beneath the sedimentary basins is progressively dissipated with increasing depth. In

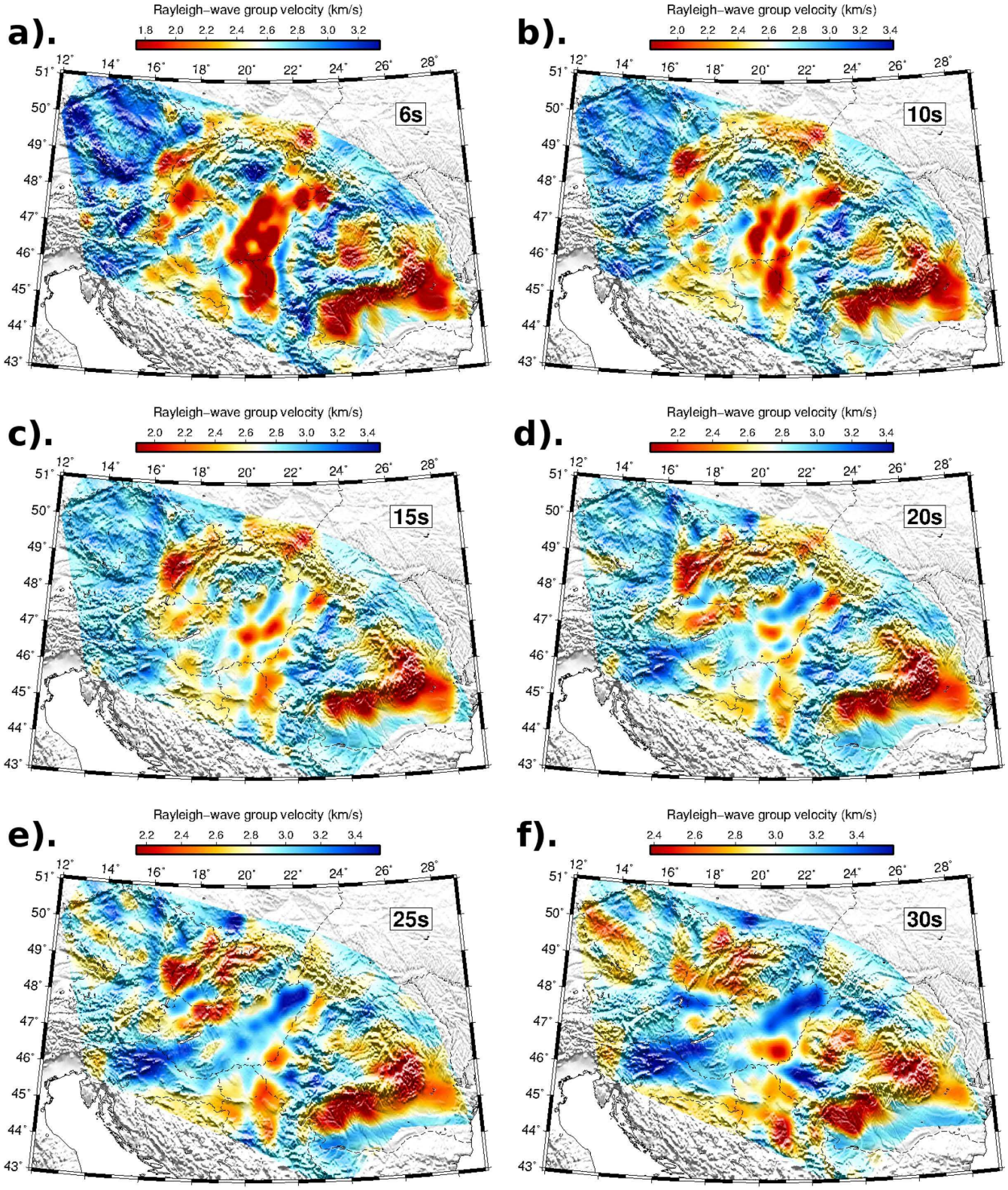

Figure 7. Inverted Rayleigh-wave group velocity maps at periods: 6, 10, 15, 20, 25 and 30 s. Note variation of colour scale between frames.

the mid to lower crust (16–30 km, Figs 11d–e), the Mid-Hungarian Line has its clearest expression as a broad NE trending relatively fast anomaly, flanked to the NW by an elongated low-velocity region beneath the Trans-Danubian Ranges. In the lower crust (Fig. 11e) the most prominent feature is a large low velocity anomaly beneath the Apuseni Mountains, but relatively low velocities also begin to appear beneath the Bohemian Massif and Eastern Alps due mainly to variations in Moho depth. Note that the maps of Fig. 11 show

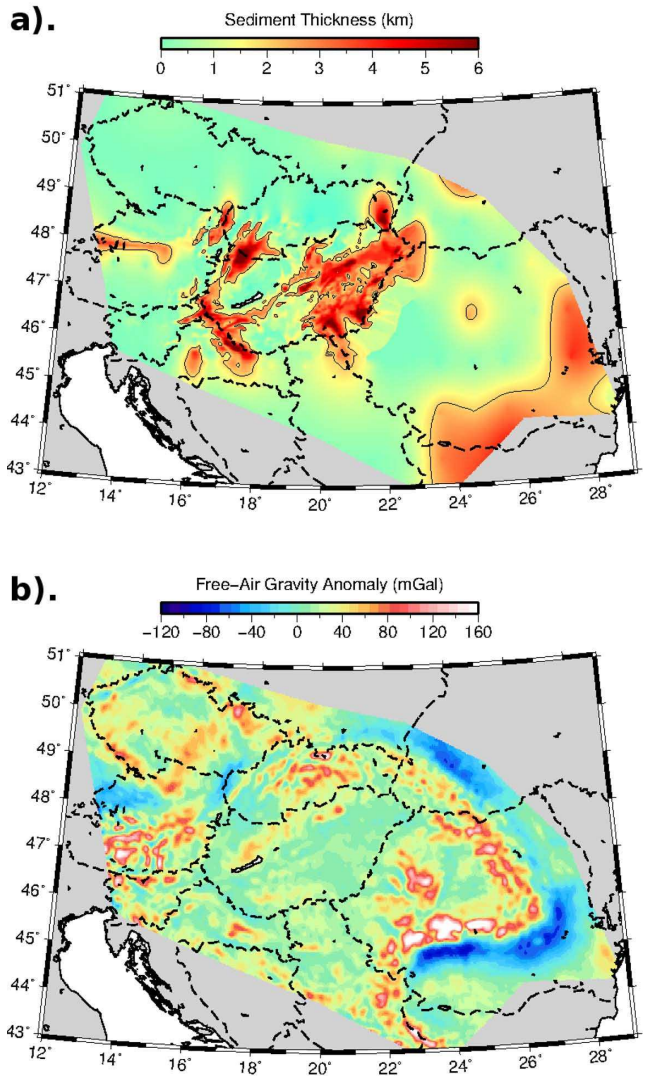

Figure 8. (a) The distribution and thicknesses of sediment in the Carpathian–Pannonian region, constructed from the compilation by Dando (2010). (b) The free-air gravity anomaly for the Carpathian–Pannonian region, constructed using Earth Gravitational Model 2008 (EGM2008) from: http://earth-info.nga.mil/GandG/wgs84/gravitymod/egm2008/index.html.

anomalous velocity relative to the horizontally averaged $V_S(z)$ profile; the white colour defines the background velocity at each depth; at 40 km (Fig. 11f) the background V_S of 3.9 km s^{-1} is close to an upper-mantle velocity.

(iii) In vertical section (Figs 12 and 13) the same lateral velocity variations are evident together with depth variations displayed using an absolute velocity scale. The most significant feature we see is attributed mainly to the variation in Moho depth, which we presume to be correlated with the model iso-velocity surface $V_S = 3.8$ km s^{-1}. The Moho is relatively shallow across the Pannonian Basin (Figs 12, B–B′ and 13, F–F′), but reaches greater depths beneath the Bohemian Massif (Fig. 12, A–A′) the Eastern Alps (Fig. 12, B–B′ and Fig. 13, C–C′), the Apuseni Mountains (Fig. 12, B–B′) and, in general, beneath the Carpathians (Fig. 13, E–E′, F–F′, G–G′)—though less so beneath the SE Carpathians (Fig. 12, B–B′). The correlation of deeper Moho and higher elevation is of course consistent with the principle of isostatic balance. However, since the depth sensitivity of the group velocity is fairly broad at the longer periods (Fig. 6) which constrain velocities at these depths, any steep gradient in velocity across the Moho is smoothed vertically and laterally. Our velocity iso-contours (Figs 12 and 13) should therefore be interpreted only as a general guide to Moho depth variation across the region.

6 DISCUSSION

Our velocity model SCP-ANT-VS1 includes numerous specific features that have been previously investigated. We briefly summarize the comparison of our model with previous geophysical experiments, focusing on prior seismological measurements; other authors will be better placed than us to apply this new velocity model to the interpretation of the many petrological, sedimentological and surface structural data which exist for this region.

6.1 Bohemian Massif and Eastern Alps

The upper crust of the Bohemian Massif is relatively fast (Figs 11a–c), but in the upper 10 km the highest velocities are found beneath the elevated rim of the Massif. In the mid-crust (16 km, Fig. 11d) a subtle band of relatively high velocity crosses the Massif, possibly related in the north to the Oligocene–Miocene Eger rift. A broad low-velocity zone below about 35 km (Fig. 12, A–A′, at the distance 50–200 km) might be related to locally thickened crust, but Grad *et al.* (2008) mapped crustal thickness varying only between about 30 and 35 km in controlled source seismic studies of the SUDETES 2003 (profile S01) experiment. Alternatively we see evidence for a broad low velocity anomaly in the upper mantle beneath the Eger rift, as reported by Plomerová *et al.* (2007) who interpreted it as an upwelling of the lithosphere–asthenosphere boundary and related it to the basaltic volcanism associated with the rift. This region in general has relatively high heat flow (Čermák & Bodri 1998; Tari *et al.* 1999; Lenkey *et al.* 2002) which may be associated with Neogene volcanism. Grad *et al.* (2008) also identified a number of high-velocity bodies in the upper crust of the Massif at depths of 4–10 km, which they interpreted as lower crustal rocks or mafic intrusions. Our model (Fig. 12, A–A′) also hints at such structures, but our inversion does not have the same high resolution locally as the reflection/refraction profile of Grad *et al.* (2008).

In the Eastern Alps, we find two distinct low velocity zones in the uppermost crust down to about 5 km depth in our *S*-wave velocity model (Fig. 13, C–C′). The low velocity anomaly below the Northern Calcareous Alps has also been reported in the seismic refraction and reflection studies that followed the CELEBRATION 2000 and ALP 2002 seismic experiments (Behm *et al.* 2007; Brückl *et al.* 2007; Hrubcová & Środa 2008; e.g. profile ALP01 in the ALP 2002 seismic experiment and joint profile CEL10 and ALP04 from CELEBRATION 2000 and ALP 2002 seismic experiments). Hrubcová & Środa (2008) attributed these low velocities to the Molasse and Helvetic Flysch sediments that were overthrust by the Northern Calcareous Alps on a SW dipping thrust during the formation of the Eastern Alps. Further south, the more prominent low velocity zone below the central part of the Eastern Alps is not previously reported. The location of this low-velocity zone corresponds to the Austroalpine basement nappes, which have been affected by Oligocene–Miocene orogen-parallel extension and normal faulting along east and west dipping low-angle detachment faults (Linzer *et al.* 2002).

The middle crust beneath the Southern Alps is characterized by relatively high velocities at depths of 20–30 km (Fig. 13, C–C′). Furthermore, the Moho appears to increase in depth southward across the Eastern Alps with the thinnest crust below the Northern

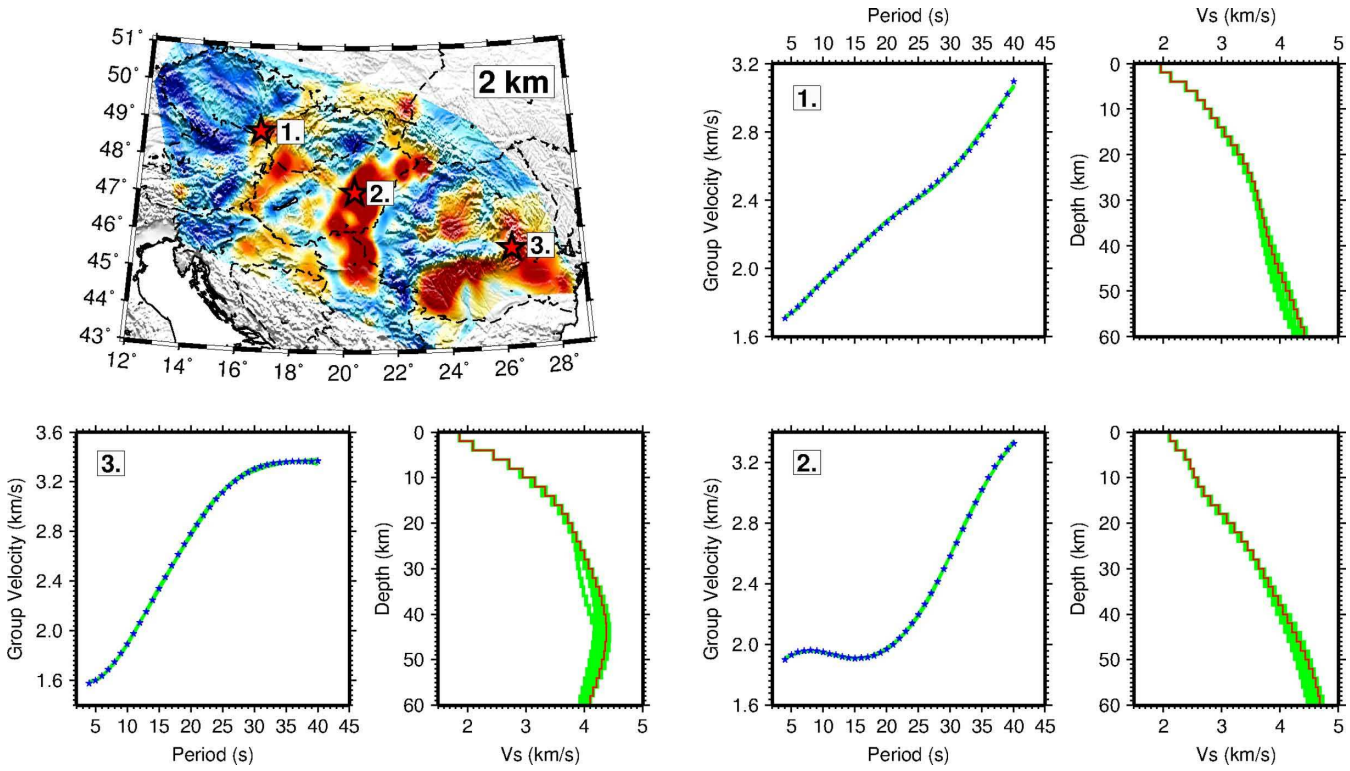

Figure 9. Examples of depth inversions for selected locations indicated by white squares in the upper left map. In the left-hand panel of each example, the blue stars show the dispersion curve obtained from the group velocity tomography and green lines show the range of predicted dispersion curves from the set of 1-D velocity models shown in the right-hand panel. In the right-hand panel of each example, green lines show the range of acceptable 1-D velocity models obtained from the inversion and the red line indicates the median solution of all 1-D velocity models for which the data misfit is less than 0.5 per cent.

Calcareous Alps, increasing in thickness below the Southern Alps to ∼47 km. This thick crust beneath the Southern Alps is consistent with the compilations of Tesauro *et al.* (2008) and Grad *et al.* (2009). However, the relatively shallow Moho we find beneath the Northern Calcareous Alps differs significantly (Fig. 13, C–C′) from the Moho depths reported by Tesauro *et al.* (2008) and Grad *et al.* (2009) in that region. The southward crustal thickening below the Eastern Alps that we find has also been reported in previous seismic reflection and refraction studies (Brückl *et al.* 2007; Hrubcová & Środa 2008).

6.2 West Carpathians and Pannonian Basin

The West Carpathians fall largely within the Alcapa unit defined by Horváth *et al.* (2006). From north to south, they include the Carpathian Foredeep, Outer Carpathians, Pieniny Klippen Belt and Inner Carpathians. The uppermost crust in the Outer Carpathians and the Carpathian Foredeep has relatively low velocities down to 10 km, attributable to the Foredeep depression filled with sedimentary rocks (Fig. 13, E–E′). This low velocity zone seems to dip to the SW to depths of about 20 km beneath the central part of the West Carpathians, as also reported in the seismic reflection and refraction studies along the profiles CEL01 and CEL04 from the CELEBRATION 2000 seismic experiment (Środa *et al.* 2006). A localized zone of very low velocities down to ∼5 km is also observed where the Pannonian region and the West Carpathians meet, coinciding with the Miocene (∼10 Ma) Central Slovakian Volcanic Field (CSVF). The crustal thickness reaches ∼40 km below the inner part of the West Carpathians but thins to the NE and SW (Fig. 13, E–E′). This variation of crustal thickness was also reported by Środa *et al.* (2006), who described a crustal root beneath the West Carpathians. However, we again note a significant difference (Fig. 13, E–E′) in our estimate of the Moho depth beneath the inner West Carpathians and the estimates published in the compilations of Tesauro *et al.* (2008) and Grad *et al.* (2009).

The Pannonian Basin, assembled from Alcapa and Tisza units, includes several basin depocentres and is crossed by the Trans-Danubian Range and the Mid-Hungarian Line. Our shear wave velocity model clearly identifies the locations of the basin depocentres and their relative depth extents. The Drava Trough and Danube Basin are associated with low velocity zones down to ∼4 and ∼6 km, respectively, whereas the low velocity zone associated with the Vienna Basin extends down to at least 12 km (Fig. 13, D–D′). The images suggest that the low velocity zone below the Vienna Basin dips to the SSW, consistent with the Vienna basin model of Lankreijer *et al.* (1995) which shows a southward deepening of the basin controlled by a major SE-dipping detachment fault. The Pannonian Basin can be divided into two parts: the northeastern part including the East Slovakian Basin (EB) and the southern part, in which the Makó Trough and Békés Basin are the two deepest subbasins. shear wave velocity models show that both subbasins extend to depths of ∼8 km (Fig. 12, A–A′ and B–B′ and Fig. 13, F–F′) consistent with seismic reflection profiles (Posgay *et al.* 2006). The crust beneath the Pannonian Basin is relatively thin, generally within the range 25–30 km, and thinnest (∼25 km) in the northeast, beneath the Békés Basin and the East Carpathians (Fig. 13, F–F′). Our crustal thickness estimates agree with previous studies in which the average thickness of the crust is reported as ∼25 km in the Pannonian region (Szafián *et al.* 1997; Horváth *et al.* 2006; Tesauro *et al.* 2008; Grad *et al.* 2009), probably resulting from a rift-dominated extension phase in the Miocene (Szafián *et al.* 1997;

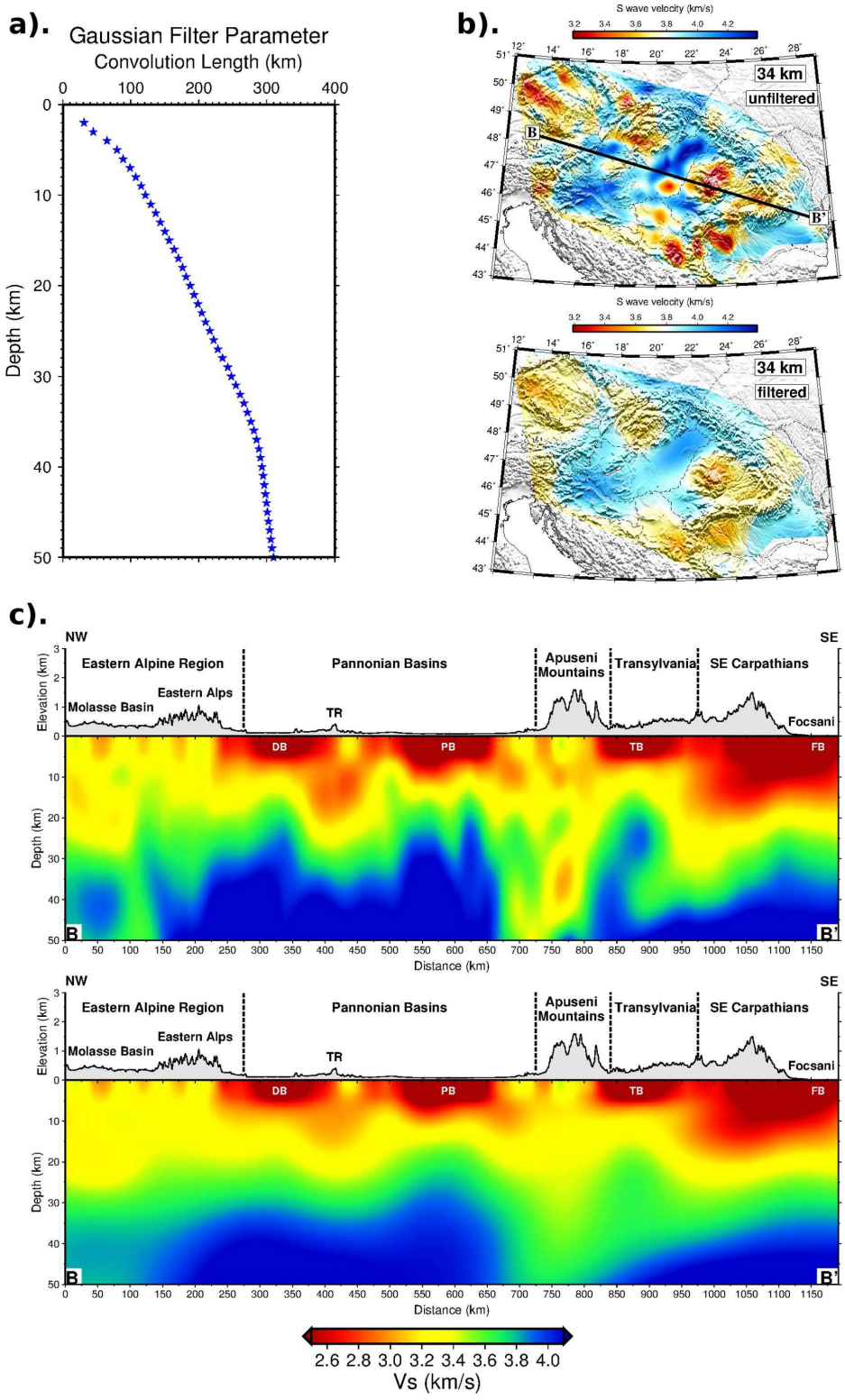

Figure 10. (a) Smoothing length of depth-dependent Gaussian filter applied to our 3-D velocity model. (b) Horizontal slices at 34 km depth for the 3-D shear wave velocity models without (top) and with (bottom) the Gaussian horizontal smoothing filter applied. (c) Vertical section through the 3-D shear wave velocity models for the profile B–B′ indicated in (b) without (top panel) and with (bottom panel) the depth-dependent Gaussian filter applied.

Huismann *et al.* 2001). Miocene lithospheric (and crustal) extension in the region is reflected in high surface heat flow values (90–100 mW m^{-2}; Lenkey *et al.* 2002). Previous analyses of the gravity field suggest that a narrow rift model with up-domed Moho caused by significant crustal extension, and possibly intrusions of mantle material into the crust during the Neogene, can explain the relatively high Bouguer gravity anomaly (∼20 mGal) of the Békés Basin (Bielik *et al.* 1991; Szafián *et al.* 1997; Bielik & Ádám 2006), consistent with the localized shallow Moho that we find in this region.

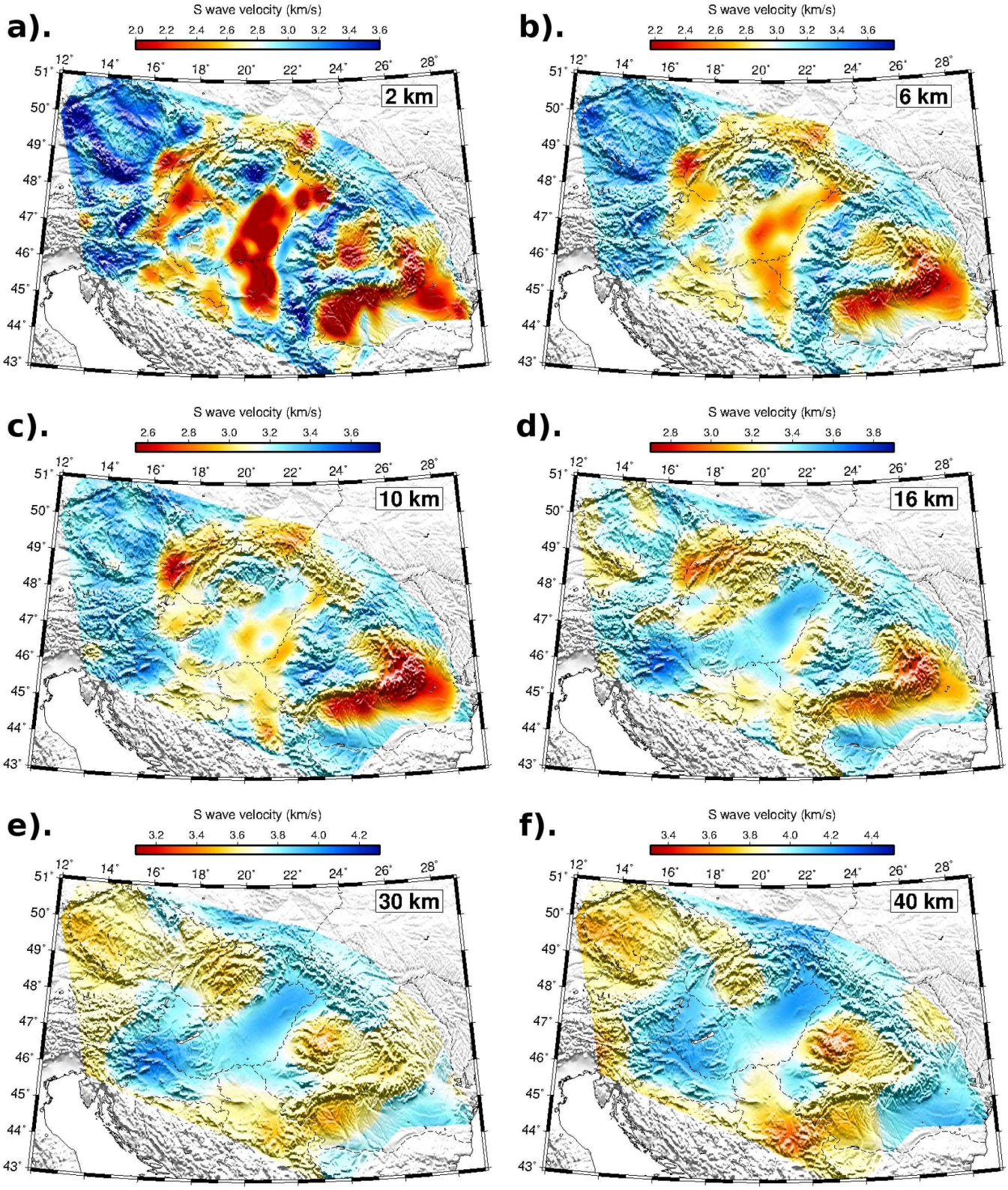

Figure 11. Horizontal slices through the 3-D shear wave velocity model SCP-ANT-VS1 at depths: 2, 6, 10, 16, 30 and 40 km. Note the changing colour scale with depth.

6.3 Transylvanian region, East and South Carpathians

The Transylvanian Basin is the major sedimentary basin in the southeastern part of the Carpathian system, bounded by the Apuseni Mountains to the west, and the Carpathians to the east and south. The Transylvanian Basin is associated with relatively low velocities down to ∼5 km depth in our shear wave velocity model (Fig. 12, B–B′ and Fig. 13, G–G′). The lower crust below the Apuseni

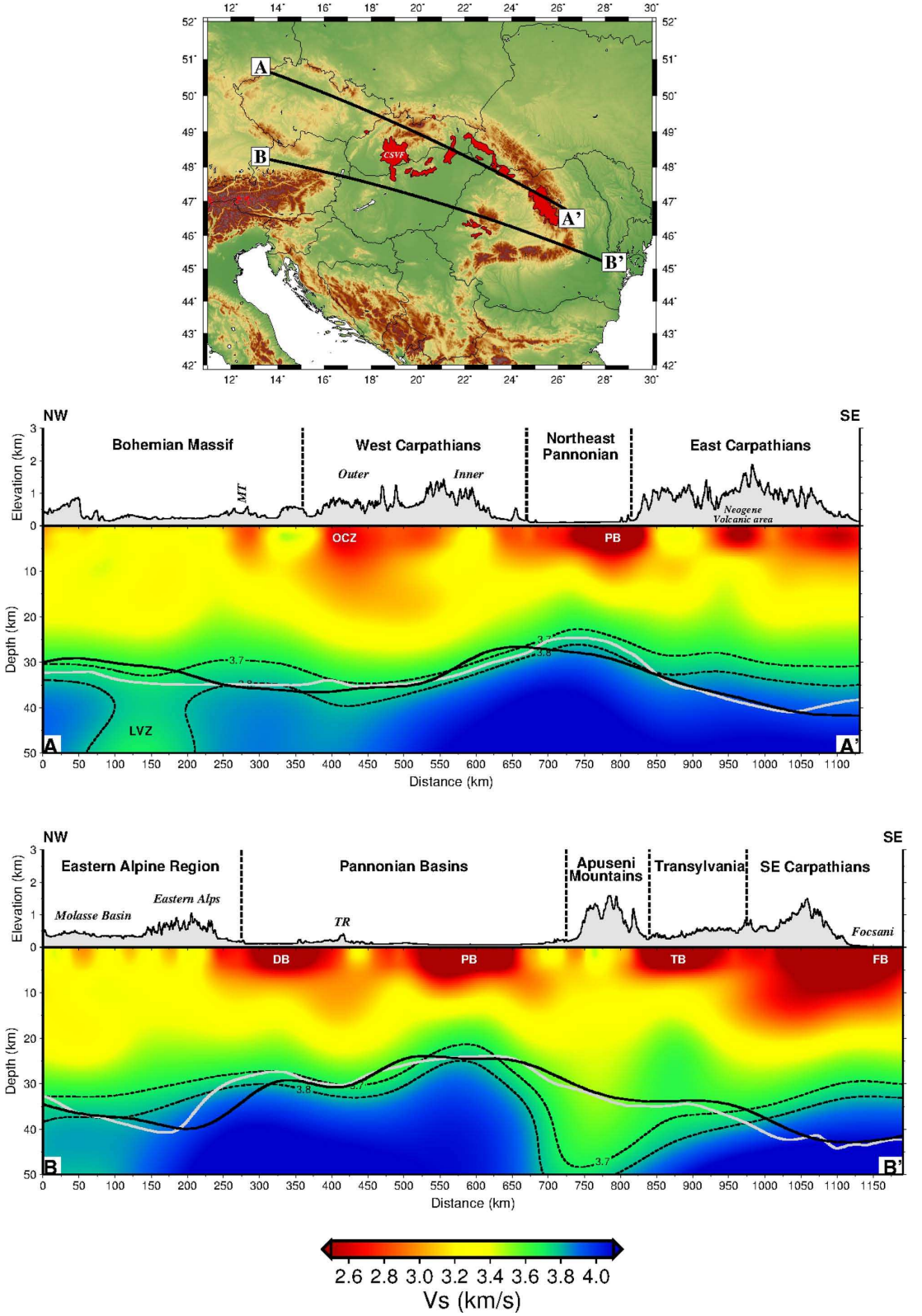

Figure 12. Vertical sections through the 3-D shear wave velocity model SCP-ANT-VS1: A–A′ and B–B′. PB, Pannonian Basin; OCZ, Outer Carpathian Zone; DB, Danube Basin; TB, Transylvanian Basin; FB, Foçsani Basin; LVZ, low velocity zone. The dashed lines shows the iso-velocities of $V_S = 3.7$ and 3.8 km s^{-1}; the grey and black continuous lines correspond to Moho depths interpolated from the models of Tesauro *et al.* (2008) and Grad *et al.* (2009), respectively. Note vertical exaggeration.

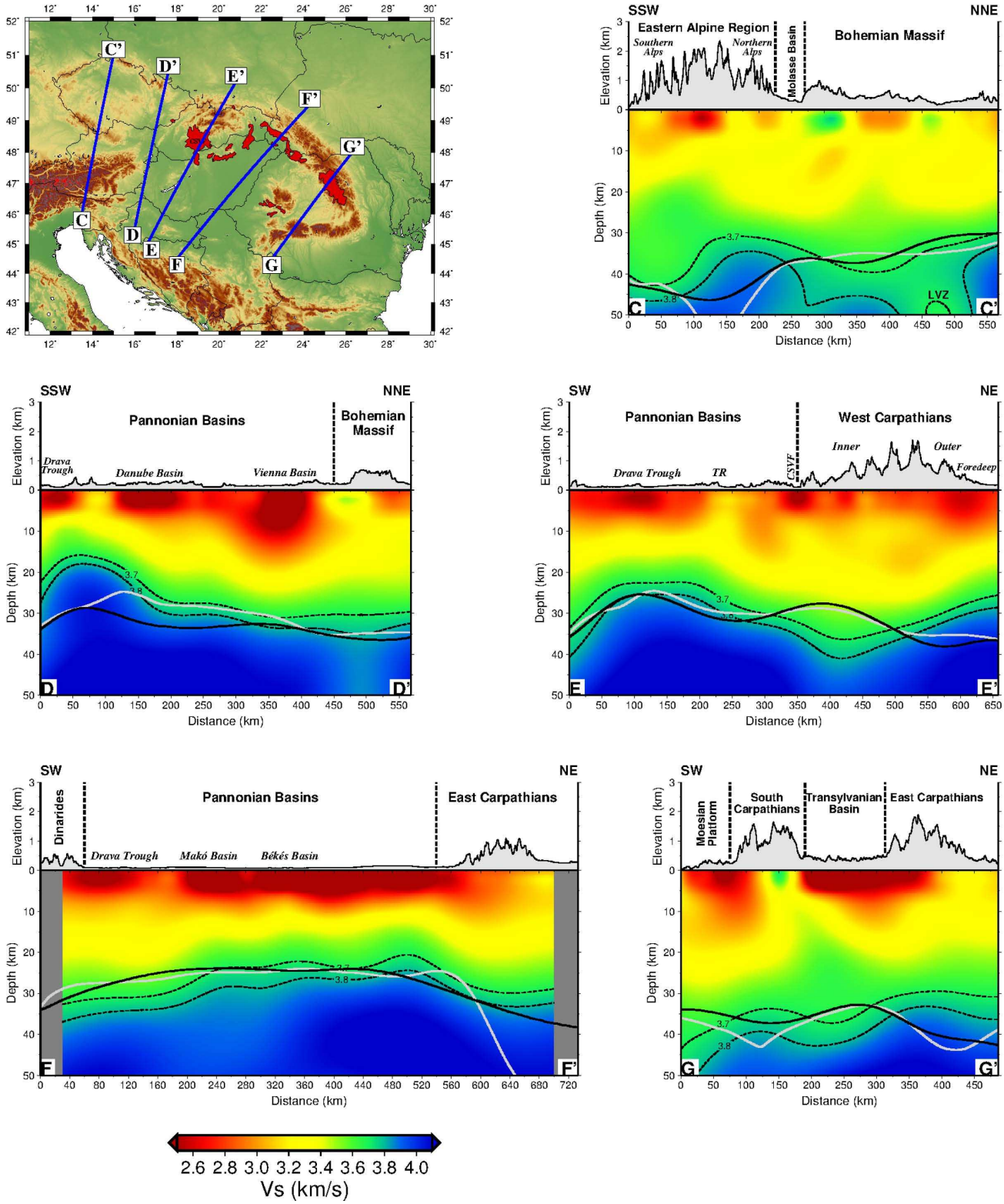

Figure 13. Vertical sections through the 3-D shear wave velocity model SCP-ANT-VS1: C–C′, D–D′, E–E′, F–F′ and G–G′. TR, Transdanubian Range; LVZ, low velocity zone. The dashed lines shows the iso-velocities of $V_S = 3.7$ and 3.8 km s^{-1}; the grey and black continuous lines correspond to Moho depths from Tesauro *et al.* (2008) and Grad *et al.* (2009), respectively. Note vertical exaggeration.

Mountains (20–40 km) is anomalously thick and relatively slow (Fig. 12, B–B′) compared to high velocities further east beneath the Transylvanian Basin. The Transylvanian Basin is, in general, associated with relatively low heat flow (26–58 mW m^{-2}, with a mean value of 38 mW m^{-2}) compared to surrounding areas (Cranganu & Deming 1996), but relatively thick crust (Horváth 1993). We estimate for the Transylvanian Basin a crustal thickness of ∼40 km (Fig. 12, B–B′

and Fig. 13, G–G′), somewhat less than the Moho depths (∼44–46 km) reported from the DRACULA I+DACIA PLAN seismic reflection studies by Fillerup *et al.* (2010). Tesauro *et al.* (2008) and Grad *et al.* (2009), however, estimated a Moho depth of about 30–35 km for the Transylvanian Basin regions. Furthermore both of those compilations have missed the thick crust we find beneath the Apuseni Mountains and conversely they find greater crustal thickness than we find beneath the SE Carpathians and the Foçsani Basin where crustal thickness decreases systematically to 30–35 km (Fig. 12, B–B′).

In the East Carpathians, the Neogene volcanic region north of the Vrancea Zone, is associated with low velocities down to ∼6 km depth (Fig. 12, A–A′). To the southeast of the Carpathians, a broad low velocity region is attributable to the foredeep zone of the Foçsani Basin with low velocities down to 10–15 km (Fig. 12, B–B′), consistent with the 15 km deep Foçsani basement inferred from the VRANCEA 2001 seismic line (Hauser *et al.* 2007). Furthermore, the section B–B′ (Fig. 12) suggests that the low velocities of the basin dip beneath the East Carpathians to the west, as if Foçsani sediments underthrust the Carpathian orogen. The upper crust of the South Carpathians is associated with a localized high velocity anomaly, which is near vertical in the upper 10 km (Fig. 13, G–G′) and contrasts strongly with the shallow (≃10 km) low velocities of the Moesian Platform (corresponding to the Dacic foredeep basin) on one side and the Transylvanian Basin on the other side. This fast structure appears coherent right through the crust, dipping to the NE beneath the Transylvanian Basin.

The East Carpathian crustal thickness increases systematically to the north from ∼32 km (Fig. 12, A–A′, B–B′) to ∼35 km (Fig. 13, F–F′, G–G′), but in general appears thinner than the estimates (∼40 km) of Tesauro *et al.* (2008) and Grad *et al.* (2009). In our model relatively thin crust (∼32 km) is found below the contact zone between the East Carpathians and Foçsani Basin, whereas measurements from the VRANCEA 2001 seismic refraction line (Hauser *et al.* 2007) and the DRACULA I+DACIA PLAN seismic reflection profile (Fillerup *et al.* 2010) suggest a crustal thickness of ∼42–45 km below the Foçsani Basin, thinning towards the NW to ∼31–33 km in the Vrancea Zone of the SE Carpathians. Finally, the thicker crust of the South Carpathians (∼40 km; Fig. 13, G–G′) is broadly consistent with the crustal root suggested by Szafián & Horváth (2006) to explain the observed low Bouguer gravity anomalies (≤−100 mgal) in the South Carpathians.

7 CONCLUSIONS

A new high-resolution shear wave velocity model for the crust of the Carpathian–Pannonian region has been obtained using tomographic inversion of Rayleigh waves at periods 4–40 s retrieved from ambient seismic noise analysis. Our group velocity maps show good quantitative agreement with known geological features. We demonstrate that Rayleigh-wave dispersion curves obtained from ambient noise correlation at periods as short as 4–8 s can image very well the sedimentary basins and their depth extents. High topographic regions are associated with high group velocities at short periods (4–8 s) corresponding to near-surface crystalline rocks and low group velocities at mid-periods (15–22 s) consistent with the thicker crust required for isostatic compensation. Long period group velocity maps (>25 s) show high velocities in the Pannonian Basin, consistent with the crustal thinning which occurred during basin extension. Our shear wave velocity model SCP-ANT-VS1 obtained from the inversion of the group velocity maps has been compared, where possible, with previous geophysical investigations. In general our new model is validated by these comparisons, but some intriguing differences are found, notably in relation to crustal thickness estimates beneath the Apuseni Mountains and the Southeast Carpathians. To summarize the main features of the model:

(i) At shallow depths (<10 km), high topographic regions like the Bohemian Massif, Eastern Alps, most of the Carpathian arc, the Apuseni Mountains and the Trans-Danubian Ranges are associated with relatively high velocities, whereas sedimentary domains like the Danube, Vienna, Pannonian, Transylvanian, Foçsani and Dacic Basins have low velocities. The low velocities associated with the Foçsani and Dacic Basins seem to intrude below the SE Carpathians (Vrancea region) and across the Moesian Platform.

(ii) The middle crust (10–16 km) beneath the Bohemian Massif and Eastern Alps is relatively fast, but most of the Carpathians and the Trans-Danubian Range are slow at these depths relative to surrounding regions, and the slow signature beneath the sedimentary basins is progressively dissipated with depth.

(iii) In the mid to lower crust (16–34 km), the Mid-Hungarian Line is associated with a broad NE trending relatively fast anomaly, flanked to the NW by an elongated region of low velocities beneath the Trans-Danubian Ranges.

(iv) At depths of 30–40 km, relatively low velocities appear beneath the Bohemian Massif and Eastern Alps but the most prominent feature is a large low velocity anomaly interpreted as anomalously thick crust beneath the Apuseni Mountains. Most of the Pannonian and Vienna Basin regions at these depths are relatively fast, presumably related to shallowing of the Moho.

(v) Our estimates of Moho depths, roughly based on the isovelocity surface $V_S = 3.8\,\mathrm{km\,s^{-1}}$, are generally consistent with results from previous studies and accord well with different tectonic features though we find specific differences relative to two recent Moho compilations of Tesauro *et al.* (2008) and Grad *et al.* (2009).

ACKNOWLEDGEMENTS

The South Carpathian Project was supported by NERC standard grant NE/G005931/1. The seismological equipment used in the SCP network was provided by SEIS-UK as the NERC Geophysical Equipment Facility. The fieldwork for the SCP project was a collaborative project between the University of Leeds, UK, Eötvös Loránd Geophysical Institute (ELGI), Budapest, Hungary, National Institute of Earth Physics (NIEP), Bucharest, Romania and the Seismological Survey of Serbia (SSS), Belgrade, Serbia. The South Carpathian Project Working Group includes: G. Houseman, G. Stuart, Y. Ren, B. Dando, P. Lorinczi, O. Gogus (University of Leeds, UK); E. Hegedüs, A. Kovács, I. Török, I. László, R. Csabafi (ELGI); C. Ionescu, M. Radulian, V. Raileanu, D. Tataru, B. Zaharia, F. Borleanu, C. Neagoe, G. Gainariu, D. Rau (NIEP); S. Radovanovic, V. Kovacevic, D. Valcic, S. Petrovic-Cacic, G. Krunic (SSS); A. Brisbourne, D. Hawthorn, V. Lane (SEIS-UK, Leicester University, UK). Data from permanent stations used in this study were obtained from the GFZ, ORFEUS and IRIS seismological data archives with additional data from the Romanian regional network provided by NIEP. The authors thank N. Rawlinson of Australian National University, for making available his 2-D non-linear inversion code, M. Schimmel for his non-linear phase weighted stacking code and R. Herrmann of Saint Louis University, St. Louis, Missouri, for providing his seismological software package, which is used for the dispersion curve inversion.

Most figures were made using GMT software (Wessel & Smith 1998). We thank Nick Rawlinson and an anonymous reviewer for their valuable comments/suggestions which improved this manuscript.

REFERENCES

Arroucau, P., Rawlinson, N. & Sambridge, M., 2010. New insight into Cainozoic sedimentary basins and Palaeozoic suture zones in southeast Australia from ambient noise surface wave tomography, *Geophys. Res. Lett.*, **37,** L07303, doi:10.1029/2009GL041974.

Bassin, C., Laske, G. & Masters, G., 2000. Current limits of resolution for surface wave tomography in North America, *EOS, Trans. Am. geophys. Un.*, **81,** F897.

Behm, M., Brückl, E., Chwatal, W. & Thybo, H., 2007. Application of stacking and inversion techniques to 3D wide-angle reflection and refraction seismic data of the Eastern Alps, *Geophys. J. Int.*, **170**(1), 275–298.

Bensen, G.D., Ritzwoller, M.H., Barmin, M.P., Levshin, A.L., Lin, F., Moschetti, M.P., Shapiro, N.M. & Yang, Y., 2007. Processing seismic ambient noise data to obtain reliable broad.band surface wave dispersion measurements, *Geophys. J. Int.*, **169,** 1239–1260.

Bielik, M., 1991. Density modelling of the Earth's crust in the Intra-Carpathian basins, in *Geodynamic Evolution of the Pannonian Basin*, Vol. 62, pp. 123–132, ed. Karamata, S., Acad. Conf. Serbian Acad. Sci. Arts.

Bielik, M. & Adám, A., 2006. Structure of the Lithosphere in the Carpathian-Pannonian Region, in *The Carpathians and Their Foreland: Geology and Hydrocarbon Resources*, pp. 699–706, eds Golonka, J. & Picha, F.J., AAPG Memoir 84.

Brückl, E. *et al.*, 2003. ALP 2002 Seismic Experiment, *Stud. Geophys. Geod.*, **47**(3), 671–679.

Brückl, E. *et al.*, 2007. Crustal structure due to collisional and escape tectonics in the Eastern Alps region based on profiles Alp01 and Alp02 from the ALP 2002 seismic experiment, *J. geophys. Res.*, **112,** B06308, doi:10.1029/2006JB004687.

Čermák, V. & Bodri, L., 1998. Heat flow map of Europe revisited, in *Mitteilungen der Deutschen Geophysikalischen Gesellschaft*, pp. 58–63, ed. Clauser, C., Sonderband II.

Cho, K.H., Herrmann, R.B., Ammon, C.J. & Lee, K., 2007. Imaging the Upper Crust of the Korean Peninsula by Surface-Wave Tomography, *Bull. seism. Soc. Am.*, **97,** 198–207.

Cranganu, C. & Deming, D., 1996. Heat flow and hydrocarbon generation in the Transylvanian basin, Romania, *AAPG Bull.*, **80**(10), 1641–1653.

Csontos, L. & Vörös, A., 2004. Mesozoic plate reconstructions of the Carpathian region, *Paleogeogr. Paleoclim. Paleoecol.*, **210,** 1–56.

Dando, B., 2010. Seismological structure of the Carpathian-Pannonian region of central Europe, *PhD thesis*, School of Earth and Environment, University of Leeds.

Dando, B.D.E., Stuart, G.W., Houseman, G.A., Hegedüs, E., Brückl, E. & Radovanović, S., 2011. Teleseismic tomography of the mantle in the Carpathian-Pannonian region of central Europe, *Geophys. J. Int.*, **186,** 11–31.

Derode, A., Larose, E., Tanter, M., de Rosny, J., Tourim, A., Campillo, M. & Fink, M., 2003. Recovering the Green's function from field-field correlations in an open scattering medium, *J. acoust. Soc. Am.*, **113,** 2973–2976.

Dziewonski, A., Bloch, S. & Landisman, M., 1969. A technique for the analysis of transient seismic signals, *Bull. seism. Soc. Am.*, **59,** 427–444.

Fillerup, M.A., Knapp, J.H., Knapp, C.C. & Raileanu, V., 2010. Mantle earthquakes in the absence of subduction? Continental delamination in the Romanian Carpathians, *Lithos*, **2**(5), 333–340.

Gemmer, L. & Houseman, G.A., 2007. Convergence and extension driven by lithospheric gravitational instability: evolution of the Alpine-Carpathian-Pannonian system, *Geophys. J. Int.*, **168,** 1276–1290.

Grad, M., Spicak, A., Keller, G.R., Guterch, A., Broz, M. & Hegedüs, E. Working Group (incl. P. Środa), 2003. SUDETES 2003 seismic experiment, *Stud. Geophys. Geod.*, **47,** 681–689.

Grad, M., Guterch, A., Mazur, S., Keller, G.R., Špičák, A., Hrubcová, P. & Geissler, W.H., 2008. Lithospheric structure of the Bohemian Massif and adjacent Variscan belt in central Europe based on profile S01 from the SUDETES 2003 experiment, *J. geophys. Res.*, **113,** B10304, doi:10.1029/2007JB005497.

Grad, M. & Tiira, T. ESC Working Group, 2009. The Moho depth map of the European Plate, *Geophys. J. Int.*, **176**(1), 279–292.

Guterch, A. *et al.*, 2003. CELEBRATION 2000 seismic experiment, *Stud. Geophys. Geod.*, **47,** 659–669.

Hauser, F., Raileanu, V., Fielitz, W., Dinu, C., Landes, M., Bala, A. & Prodehl, C., 2007. Seismic crustal structure between the Transylvanian Basin and the Black Sea, Romania, *Tectonophysics*, **430,** 1–25.

Herrmann, R.B. & Ammon, C.J., 2004. *Computer programs in seismology—3.30: GSAC—generic seismic application coding*, Available at: http://www.eas.slu.edu/eqc/eqccps.html (last accessed 2013).

Horváth, F., 1993. Towards a mechanical model for the formation of the Pannonian basin, *Tectonophysics*, **226,** 333–357.

Horváth, F., Bada, G., Szafián, P., Tari, G., Ádám, A. & Cloetingh, S., 2006. Formation and deformation of the Pannonian Basin: constraints from observational data, in *European Lithosphere Dynamics*, Vol. 32 pp. 191–206, eds Gee, D. & Stephensen, R., Geological Society of London Memoirs, Geological Society of London.

Houseman, G.A. & Gemmer, L., 2007. Intra-orogenic extension driven by gravitational instability: Carpathian-Pannonian orogeny, *Geology*, **35**(12), 1135–1138.

Hrubcová, P. & Środa, P. CELEBRATION 2000 Working Group, 2008. Crustal structure at the easternmost termination of the Variscan belt based on CELEBRATION 2000 and ALP 2002 data, *Tectonophysics*, **460,** 55–75.

Huismans, R.S., Podladchikov, Y.Y. & Cloetingh, S., 2001. Dynamic modeling of the transition from passive to active rifting, application to the Pannonian basin, *Tectonics*, **20**(6), 1021–1039.

Ivan, M., 2011. Crustal thickness in Vrancea area, Romania from *S* to *P* converted waves, *J. Seismol.*, **15,** 317–328.

Kang, T.S. & Shin, J.S., 2006. Surface-wave tomography from ambient seismic noise of accelerograph networks in southern Korea, *Geophys. Res. Lett.*, **33,** L17303, doi:10.1029/2006GL027044.

Kennett, B.L.N., Sambridge, M. & Williamson, P.R., 1988. Subspace methods for large scale inverse problems involving multiple parameter classes, *Geophys. J. Int.*, **94,** 237–247.

Kovács, I. & Haas, J., 2011. Displaced South Alpine and Dinaridic elements in the mid-Hungarian zone, *Central Eur. Geol.*, **53**(2), 135–164.

Lankreijer, A., Kovács, M., Cloetingh, S., Pitonak, P., Hloska, M. & Biermann, C., 1995. Quantitative subsidence analysis and forward modelling of the Vienna and Danube basins: thin-skinned versus thick-skinned extension, *Tectonophysics*, **252,** 433–451.

Larose, E., Derode, A., Corennec, D., Margerin, L. & Campillo, M., 2005. Passive retrieval of Rayleigh waves in disoredered elastic media, *Phys. Rev. E.*, **72,** 046607, doi:10.113/PhysRevE.72.046607.

Leever, K.A., 2007. Foreland of the Romanian Carpathians Controls on late orogenic sedimentary basin evolution and Paratethys paleogeography, *PhD thesis*, Vrije Universiteit Amsterdam.

Lenkey, L., Dövényi, P., Horváth, F. & Cloetingh, S., 2002. Geothermics of the Pannonian basin and its bearing on the neotectonics, *EGU Stephen Mueller Spec. Publ. Ser.*, **3,** 29–41.

Li, H.Y., Su, W., Wang, C.Y. & Huang, Z.X., 2009. Ambient noise Rayleigh wave tomography in western Sichuan and eastern Tibet, *Earth planet. Sci. Lett.*, **282,** 201–211.

Lin, F.C., Ritzwoller, M.H., Townend, J., Savage, M. & Bannister, S., 2007. Ambient noise Rayleigh wave tomography of New Zealand, *Geophys. J. Int.*, **72**(2), 649–666.

Linzer, H.G., Decker, K., Peresson, H., DellMour, R. & Frisch, W., 2002. Balancing orogenic float of the Eastern Alps, *Tectonophysics*, **354,** 211–237.

Martin, M., Ritter, J.R. & the CALIXTO working group, 2005. High-resolution teleseismic body-wave tomography beneath SE Romania—I. Implications for three-dimensional versus one-dimensional crustal correction strategies with a new crustal velocity model, *Geophys. J. Int.*, **162,** 448–460.

Márton, E. & Fodor, L., 1995. Combination of paleomagnetic and stress data—a case study from North Hungary *Tectonophysics*, **242,** 99–114.

Moschetti, M.P., Ritzwoller, M.H. & Shapiro, N.M., 2007. Surface wave tomography of the western United States from ambient seismic noise: Rayleigh wave group velocity maps, *Geochem. Geophys. Geosyst.*, **8,** Q08010, doi:/10.1029/2007GC001655.

Pâtraşcu, S., Panaiotu, C., Seclaman, M. & Panaiotu, C.E., 1994. Timing of rotational motion of Apuseni Mountains (Romania)—paleomagnetic data from Tertiary magmatic rocks, *Tectonophysics*, **233**(3/4), 163–176.

Plomerová, J., Achauer, U., Babuška, V. & Vecsey, L. BOHEMA working group, 2007. Upper mantle beneath the Eger Rift (Central Europe): plume or asthenosphere upwelling?, *Geophys. J. Int.*, **169**(2), 675–682.

Posgay, K., Bodoky, T., Hajnal, Z., Tóth, T.M., Fancsik, T., Hegedüs, E., Kovács, A.Cs. & Takác, E., 2006. Interpretation of subhorizontal crustal reflections by metamorphic and rheologic effects in the eastern part of the Pannonian Basin, *Geophys. J. Int.*, **167,** 187–203.

Rawlinson, N. & Sambridge, M., 2003. Seismic traveltime tomography of the crust and Lithosphere, *Adv. Geophys.*, **46,** 81–198.

Rawlinson, N. & Sambridge, M., 2004a. Wave front evolution in strongly heterogeneous layered media using the fast marching method, *Geophys. J. Int.*, **156,** 631–647.

Rawlinson, N. & Sambridge, M., 2004b. Multiple reflection and transmission phases in complex layered media using a multistage fast marching method, *Geophysics*, **69**(5), 1338–1350.

Ren, Y. *et al.*, 2012. Upper mantle structures beneath the Carpathian–Pannonian region: implications for geodynamics of the continental collision, *Earth planet. Sci. Lett.*, **349–350,** 139–152.

Royden, L.H., Horváth, F. & Burchfiel, B.C., 1982. Transform faulting, extension, and subduction in the Carpathian Pannonian Region, *Geol. soc. Am. Bull.*, **93,** 717–725.

Sabra, K.G., Gerstoft, P., Roux, P., Kuperman, W.A. & Fehler, M.C., 2005. Surface wave tomography from microseisms in Southern California, *Geophys. Res. Lett.*, **32,** L14311, doi:10.1029/2005GL023155.

Saygin, E. & Kennett, B.L.N., 2012. Crustal structure of Australia from ambient seismic noise tomography, *J. geophys. Res.*, **117,** B01304, doi:10.1029/2011JB008403.

Schimmel, M., Stutzmann, E. & Gallart, J., 2010. Using instantaneous phase coherence for signal extraction from ambient noise data at a local to a global scale, *Geophys. J. Int.*, **184,** 494–506.

Seghedi, I. *et al.*, 2004. Neogene "Quaternary magmatism and geodynamics in the Carpathian" Pannonian region: a synthesis, *Lithos*, **72**(3–4), 117–146.

Sethian, J.A. & Popovici, A.M., 1999. 3-D traveltime computation using the fast marching method, *Geophysics*, **64,** 516–523.

Shapiro, N.M., Campillo, M., Stehly, L. & Ritzwoller, M.H., 2005. High-resolution surface-wave tomography from ambient seismic noise, *Science*, **307,** 1615–1618.

Snieder, R., 2004. Extracting the Green's function from the correlation of coda waves: a derivation based on stationary phase, *Phys. Rev. E*, **69,** doi:10.1103/PhysRevE.69.046610.

Środa, P. *et al.*, 2006. Crustal and upper mantle structure of the Western Carpathians from CELEBRATION 2000 profiles CEL01 and CEL04: seismic models and geological implications, *Geophys. J. Int.*, **167,** 737–760.

Szabó, C., Harangi, S. & Csontos, L., 1992. Review of Neogene and Quaternary volcanism of the Carpathian-Pannonian region, *Tectonophysics*, **208,** 243–256.

Szafián, P., Horváth, F. & Cloetingh, S.A.P.L., 1997. Gravity contraints on the crustal structure and slab evolution along a Transcarpathian transect, *Tectonophysics*, **272,** 233–248.

Szafián, P. & Horváth, F., 2006. Crustal structure in the Carpatho-Pannonian region: insights from three-dimensional gravity modelling and their geodynamic significance, *Int. J. Earth Sci.*, **95,** 50–67.

Tari, G., Dövényi, P., Dunkl, I., Horváth, F., Lenkey, L., Stefanescu, M., Szafián, P. & Tóth, T., 1999. Lithospheric structure of the Pannonian basin derived from seismic, gravity and geothermal data, *Geol. Soc. Lond., Spec. Publ.*, **156,** 215–250.

Tesauro, M., Kaban, M.K. & Cloetingh, S.A.P.L., 2008. EuCRUST-07: a new reference model for the European crust, *Geophys. Res. Lett.*, **35,** L05313, doi:10.1029/2007GL032244.

Wapenaar, K., 2004. Retrieving the elastodynamic Green's function of an arbitrary inhomogeneous medium by cross correlation, *Phys. Rev. Lett.*, **93,** doi:10.1103/PhysRevLett.93.254301.

Weaver, R.L. & Lobkis, O.I., 2004. On the emergence of the Green's function in the correlations of a diffuse field, *J. acoust. Soc. Am.*, **116,** 2731–2734.

Williamson, P.R., 1990. Tomographic inversion in reflection seismology, *Geophys. J. Int.*, **100,** 255–274.

Williamson, P.R. & Worthington, M.H., 1993. Resolution limits in ray tomography due to wave behavior: numerical experiments, *Geophysics*, **58**(5), 727–735.

Yang, Y., Ritzwoller, M.H., Levshin, A.L. & Shapiro, N.M., 2007. Ambient noise Rayleigh wave tomography across Europe, *Geophys. J. Int.*, **168,** 259–274.

Yao, H.J., van der Hilst, R.D. & de Hoop, M.V., 2006. Surface-wave array tomography in SE Tibet from ambient seismic noise and two-station analysis—I. Phase velocity maps, *Geophys. J. Int.*, **166,** 732–744.

SUPPORTING INFORMATION

Additional Supporting Information may be found in the online version of this article:

1. sup-0001-readme.txt
2. sup-0002-SCP-ANT-VS1-0.2x0.2.dat
3. sup-0003-SCP-ANT-VS1-0.05x0.05.dat
(http://gji.oxfordjournals.org/lookup/suppl/doi:10.1093/gji/ggt316/-/DC1).

Please note: Oxford University Press is not responsible for the content or functionality of any supporting materials supplied by the authors. Any queries (other than missing material) should be directed to the corresponding author for the article.